



# Linear Friction Welding of Similar and Dissimilar Materials: A Review

Namrata Gangil<sup>1,2</sup> · Aakash Mishra<sup>1</sup> · Nadeem Fayaz Lone<sup>3</sup> · Dhruv Bajaj<sup>3</sup> · Daolun Chen<sup>3</sup> · Julfikar Haider<sup>4</sup> · Xizhang Chen<sup>5</sup> · Sergey Konovalov<sup>6</sup> · Arshad Noor Siddiquee<sup>7</sup> 

Received: 23 December 2023 / Accepted: 18 June 2024

© The Author(s) under exclusive licence to The Korean Institute of Metals and Materials 2024

## Abstract

Linear friction welding (LFW) has distinction of being a unique process which can join components in a variety of materials, shape and size configurations in an extremely low cycle time. The conventional arc welding, friction stir welding and rotary friction welding are also very popular and a lot of work has been reported on materials joined by these processes. The ability to join huge and small size parts, in a variety of similar and dissimilar materials, shapes and sizes make LFW un-paralleled. Such joint configurations are very common in transportation sectors including aerospace and railways. Very little work is reported on the LFW process in comparison to aforementioned popular welding processes. An attempt is made in this article to present the state of the art on LFW of various materials in similar and dissimilar combinations. Materials in promising applications such as space, aircraft, aerospace and railways are the main focusses. This work is expected to act as a single window to showcase all aspects of LFW on ferrous and non-ferrous materials in similar and dissimilar combinations. The manuscript begins with an overview on the principle of operation and classification, and subsequently extends the topic to detailed discussion on the joint characteristics, microstructure, material combination and application domain. The literature on LFW was studied and classified based on similar and dissimilar materials, effects of parameters on properties and microstructure responses, evolution of heat and stress conditions, and applications. The article presents, at the end, a meticulously carved out concluding summary which is expected to provide future directions and also an easy to figure out coverage on the discussion.

**Keywords** Linear friction welding · Aerospace alloys · Steels · Aluminum alloys · Welded joint properties

## 1 Background and Principle of Linear Friction Welding

The fillip on waste, energy, material and literally the reduction of all resources without compromising safety and quality has shifted the onus on energy efficient, high productivity autogenous welding processes. The solid-state welding (SSW) is distinguished among all welding techniques. In the case of fusion welding, the parent materials melt and get resolidified to make the joint. Solidification is a phase equilibrium-based process, due to which not all materials can readily join together. Further, as initial, and final states of base-alloys are the same, the intermediate fusion becomes redundant, and melting and re-solidification both introduce risk of admitting impurities and defects. In the case of solid-state welding the bonding is obtained by solid-state diffusion, which supports the joining of metallurgically non-compatible materials as well. The pressure applied during LFW expels the contaminated material from

✉ Arshad Noor Siddiquee  
arshadnsiddiquee@gmail.com

<sup>1</sup> Department of Mechanical Engineering, Ajay Kumar Garg Engineering College, Ghaziabad 201015, India

<sup>2</sup> AKGEC Skills Foundation, Ajay Kumar Garg Engineering College, Ghaziabad 201015, India

<sup>3</sup> Department of Mechanical, Industrial and Mechatronics Engineering, Toronto Metropolitan University, 350 Victoria Street, Toronto, ON M5B 2K3, Canada

<sup>4</sup> Department of Engineering, Faculty of Science and Engineering, Manchester Metropolitan University, Manchester, UK

<sup>5</sup> School of Mechanical and Electrical Engineering, Wenzhou University, Wenzhou, China

<sup>6</sup> Siberian State Industrial University, Kemerovo, Russia

<sup>7</sup> Department of Mechanical Engineering, Jamia Millia Islamia, New Delhi 110025, India

the interface in the form of flash. A constant welding pressure continuously feeds the soft material and brings out virgin material which creates sound weld [1]. The SSW processes are generally autogenous, energy input is less, free from affluent and requirement of skill, and are closer to sustainable welding. The SSW is attracting huge interest and is gradually subsuming many application domains of the conventional fusion welding. The cold welding is a case of SSW that requires little or no heat to join. At the basic level, the SSW is classified as cold welding (CW) [2], roll welding (ROW) [3], pressure welding (PW) [4], diffusion welding (DFW) [5], forge welding (FOW) [6], friction welding (FW) [7], friction stir welding (FSW) [8, 9], explosive welding (EXW) [10] and ultrasonic spot welding (USW) [11], etc. The FW stands out because of its ability to join robust sections simple and complex in shape in a single go, whereas most other processes are more suited for the flat products.

During FW, simultaneous application of pressure and relative motion generates frictional heat between mating surfaces, which softens the material at the interfaces. The contaminated interface gets softened and expelled in the form of flash and, hot virgin material is exposed to make sound joint [12]. FW is widely used to produce joints in many industrial sectors including automobile, marine and submarine, heavy engineering, aeronautical as well as railways and rapid transport systems. The FW is further

classified as rotary friction welding (RFW) [12, 13], orbital friction welding (OFW) [14] and linear friction welding (LFW) [15–18]. RFW is suitable to weld parts with rotational symmetry. During RFW, one of the components is stationary and the other is rotated while in mutual contact. In the case of OFW, the two components being joined are brought in coaxial contact and rotated about their axes at the same speed in the same direction under an axial pressure. Subsequently, an axial offset is given to provide the orbital motion [14].

In the case of LFW, one of the components is held stationary and the other oscillates at a high frequency. The two components are brought in contact under a welding pressure applied to the fixed component. Frictional heat softens the interface and after sufficient softening takes place, the oscillation is stopped, and a high upsetting force is applied for a short duration. The upsetting pressure causes the flash to come out and the interface bonding is created [15–18]. A simplified schematic of LFW process is shown in Fig. 1a.

The LFW is mainly complete in six different phases as shown in Fig. 1b. The first phase involves clamping of parts; followed by bringing the parts close to each other and the machine is brought to zero datum. In the third phase, the frequency of oscillation is ramped up and the materials make contact under an axial welding pressure. In the friction phase, the frictional heat is generated at the interface. The friction phase, per se, comprises of three sub-stages (Fig. 2),

**Fig. 1** LFW process (a) Schematic representation, (b) Steps involved in LFW

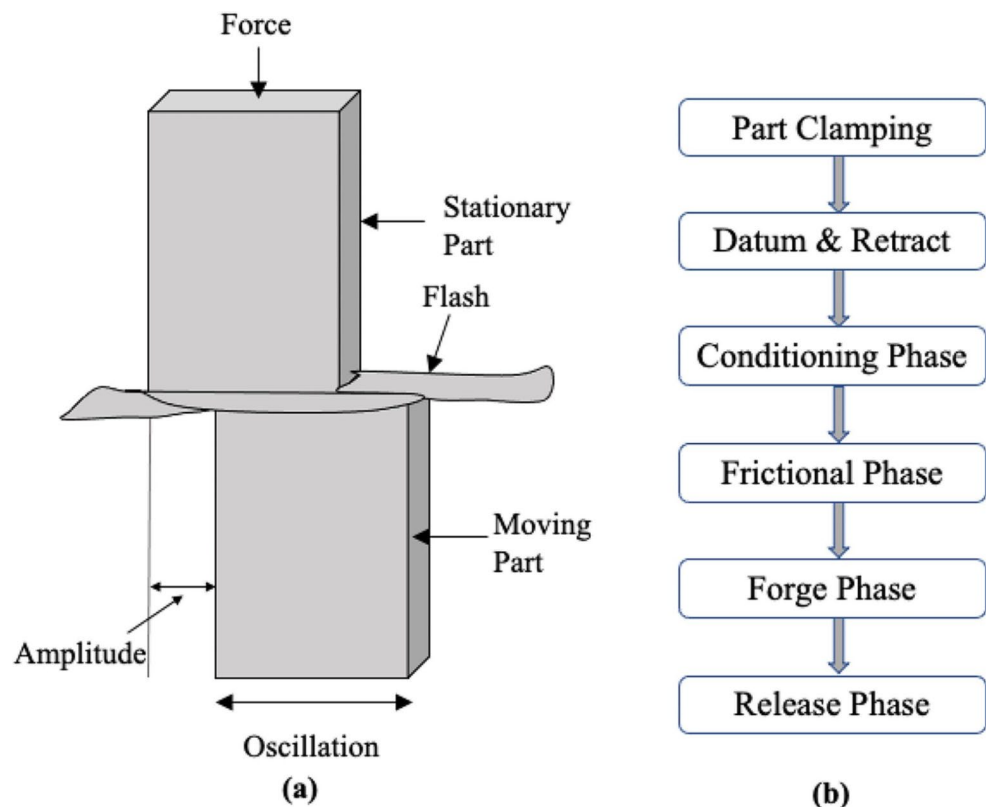
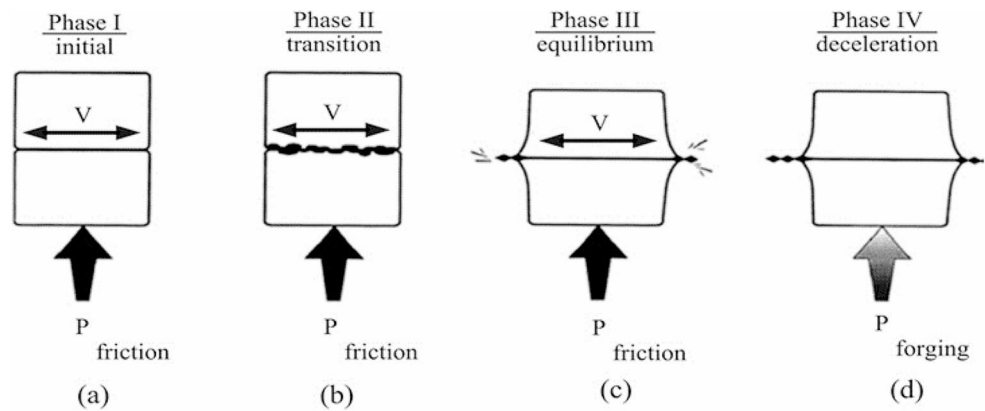


**Fig. 2** The LFW process: (a) initial phase, (b) transition phase, (c) equilibrium phase and (d) deceleration (forging phase) [22]. Reproduced with permission from Elsevier



namely initial, transition and equilibrium. The deceleration and forging are simultaneous. The heat softens the interface material and some of the softened material is expelled in the form of flash. In the fifth stage, the frequency is ramped down and the pieces are brought to rest. The application of a high upsetting or forging pressure results in the joining of workpieces. The sixth phase mainly includes the unclamping and removal of the welded product [15–18]. An LFW system is available which can operate with various amplitudes at frequencies of the order of up to 1 kHz. This system can monitor stress and temperature [19]. The evolution of temperature depends on several factors including LFW process parameters, thermal and mechanical properties of materials in addition to the cross section of the parts. The temperature can be measured by placing thermocouple, laser or infra-red sensors or thermal imaging, etc. [19–21]. The LFW system developed by Viaris and Frost [19] utilized thermocouple to measure the temperature. The thermocouple was placed at a distance of 0.7 mm from the interface. In the case of LFW of Ti6Al4V parts, 10 mm x 6 mm in cross section, performed at 10 Hz, a peak temperature of 630 °C was recorded. When the friction pressure was increased, the peak temperature increased to 840 °C [19]. In the case of medium carbon steel parts (5 mm x 25 mm in cross section), a temperature of as high as 1100 °C was recorded during LFW performed at 50 MPa and 50 Hz [21].

The heat generation takes place due to the breakdown of asperities present on the surfaces and it concludes with the increase in area of contact to approximately 100%. In the transition stage, the interface temperature rises. As the strength of materials is inversely proportional to temperature; the interface material gets softened and plastic deformation takes place. In the equilibrium stage, applied pressure and oscillation of the material results in the expulsion of the softened material in the form of flash [18, 22].

The LFW process is gaining industrial as well as scientific interest due to several attractive characteristics. In contrast to other solid-state welding processes, the ‘self-cleaning’ nature of LFW is more pronounced [23], i.e., the

surface-oxides and weld-impurities are ejected from the weld with the flash generation. This also allows LFW to be carried out in ambient conditions, without any vacuum/shielding gas which is commonly required for conventional welding processes, thereby minimizing the weld-preparation operations. Furthermore, the durability, wear and hot stresses of welding tools are a major concern for the FSW process [24], while the absence of a welding tool enables the welding of high-temperature materials using LFW which also saves the tool-production and material costs. Likewise, during USW the sonotrode tips of ultrasonic-welders may undergo damage during welding of high-strength materials. The short welding time and high repeatability of LFW [25, 26] is also appealing for mass-production. Although the rotary friction welding is largely suitable for components with circular cross-section, LFW can be adapted for axially asymmetric parts, which adds process flexibility for the production engineers [27].

A number of researchers have investigated various aspects of joining similar and dissimilar materials by LFW to-date. Studies on similar materials including pure titanium [22], titanium alloys [28], austenitic steels [29], medium carbon steels [30], aluminum alloys [31, 32], Ni-based super alloys [33], etc. have been reported. Welding of dissimilar materials include different titanium Alloys: Ti-6Al-4 V and Ti-6Al-2Sn-4Zr-2Mo-0.1Si [34], AISI316L stainless steel and Zircaloy-4 [35], FGH4096 and GH4169 superalloys [36], dissimilar aluminum alloys [37], Al-alloy AA1050 to Copper [38], Al-alloy AA6082-T6 to Mg-alloy AZ31 [39], aluminum alloy to stainless steel (AISI304) [40], Al alloy to composites [41], and superalloy IN718 to Ti6Al4V [42], etc. The timeline of oscillation, force, temperature, and burn-off distance during LFW is typically depicted in Fig. 3.

It should be noted that industry scale robust and bulk products can be joined by LFW effectively. However, the joining of thin sections is challenging and needs especial arrangements [43]. The welding of parts with thicknesses of the order of 5 mm to 20 mm by LFW has been reported in the literature with an odd investigation reported smaller

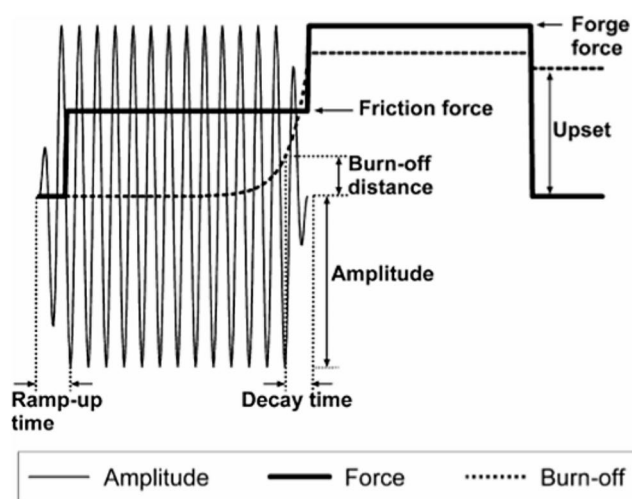


**Fig. 3** Schematic diagram of the parameters traces that are obtained during LFW [29]. Reproduced with permission from Elsevier

thickness of 2.6 mm as well [30]. It has been reported that parts with thicknesses as small as 2 mm can be welded by special low temperature LFW [44].

**Heat Input and Microstructural Zones** Specific power input ( $Q_{SPI}$ ) can be estimated in terms of combined effects of LFW parameters as given by the Eq. (1) [32].

$$Q_{SPI} = (P_{fr} \cdot f \cdot \alpha) / 2\pi \quad (1)$$

where  $P_{fr}$  is the friction pressure,  $\alpha$  is the amplitude and  $f$  is the frequency of oscillation. During LFW, the material experiences shear, axial pressure and frictional heat. Typical microstructural zones produced during LFW are weld centre zone (WCZ), thermo-mechanically affected zone (TMAZ), heat-affected zone (HAZ) and parent material (PM). Grains in WCZ generally appear very fine yet elongated; in TMAZ the grains are heavily elongated. The HAZ comprises of coarser grains, and in PM there is no change in the grains morphology.

The combinations of materials, both the similar and dissimilar, the effects of process parameters and research findings have been discussed in this paper at length. The same is organized in ease to browse through manner, for the ready reference of researchers and practitioners. The objective of this paper is to present highly relevant and comprehensive information about the linear friction welding process and its investigation on various materials. Given the paucity of reviews on the LFW process in the available scientific literature, the current work is likely to enhance the exposure of this solid-state welding process to engineers in industry and also to highlight new avenues of research and development in this area.

## 2 Linear Friction Welding of Similar Materials

Parts having similar or dissimilar shapes and sizes, made from the same materials, and finding applications in aircraft, aerospace, ship and automobile sectors have been successfully joined by LFW. The process is flexible to accommodate sizes ranging from as small as less than a kg to several tonnes. Typical examples include, turbine blades joined to disc (BLISK), age-hardened ribs of aircraft wings and Ti-tabs joined to rocket fuel tanks, etc. This section presents the details of LFW of similar materials such as aluminum alloys, Ni-based alloys, commercially pure titanium (Cp-Ti), Ti-based alloys, and stainless steel, etc.

### 2.1 LFW of Titanium and its Alloys

Titanium finds applications in aero-engines, airframe brackets, aerospace and liquefied gas storage, etc., because of its excellent properties at extreme temperatures, corrosion resistance and high specific strength, etc. [45–47]. The commercially pure titanium (Cp-Ti) is also suitable for applications in orthopaedic and dental implants. Ti has HCP structure ( $\alpha$ ) which transforms to BCC ( $\beta$ ) at 980 °C (known as  $\beta$  transus). Generally,  $\alpha$ -Titanium is stronger but less ductile, and  $\beta$ -Titanium is more ductile. The properties of  $\alpha + \beta$  phase Titanium lie in-between both. The Ti-6Al-4 V (or Ti-64) is one of the most versatile alloys among all Ti-alloys. The application of this alloy constitutes about 50% of all the Ti-alloys. Apart from high corrosion resistance, its strength-to-weight ratio is excellent [45–47]. The aeroengine parts are made to near-net shape by LFW because of excellent joint integrity, it significantly reduces buy-to-fly ratio and the process cycle time is very short. Further, the aerospace industry is rapidly adopting additively-manufactured (AM) metallic components. The LFW of Ti6Al4V parts, which were made by electron beam melting based AM process, showed that the LFW can produce joints with properties comparable to AMed base material [48]. The in-plane flash and out-of-plane flash are extruded in all four directions (Fig. 4a) due to the combined effect of frictional pressure, oscillation and heat. The amount of extruded flash is several orders of magnitude less than chips produced when the same part is made by machining [28, 45]. The LFW of Ti, because of its low thermal conductivity and high strength, can be completed within a friction time ranging from 0.5 s to 4 s [22]. The grains in LFWed joint in Cp-Ti get deformed and appear elongated in WCZ and TMAZ across the weld line (Fig. 4b). Microstructural investigation of the quenched Cp-Ti specimens, welded at different friction times, reveals that the recrystallization could only occur when the friction time was 4 s (Fig. 5a).

**Fig. 4** LFW specimens showing (a) in-plane and out-of-plane flash [28], and (b) macrostructure across the cross-section of LFWed joint of pure Ti at a friction time of 4 s showing the joint morphology [22]. Reproduced with permission from Elsevier and MDPI

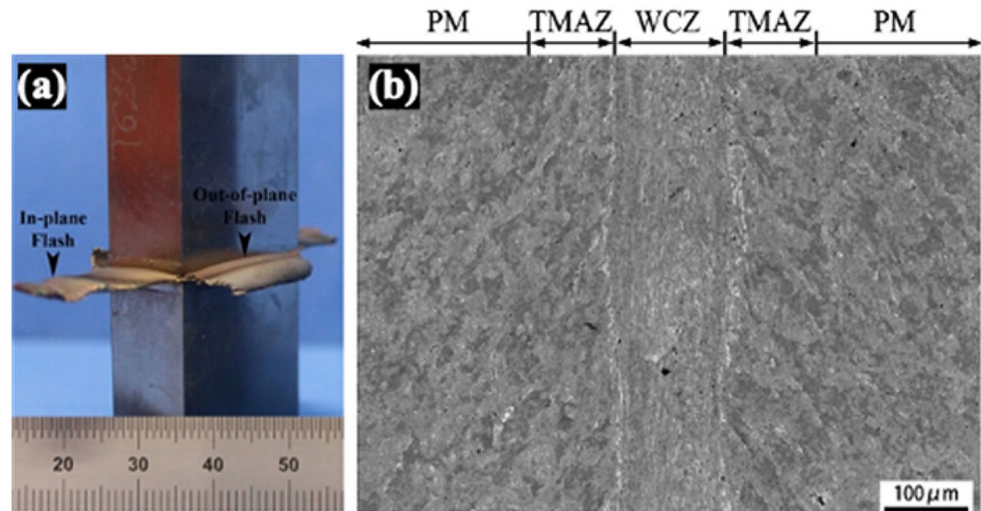
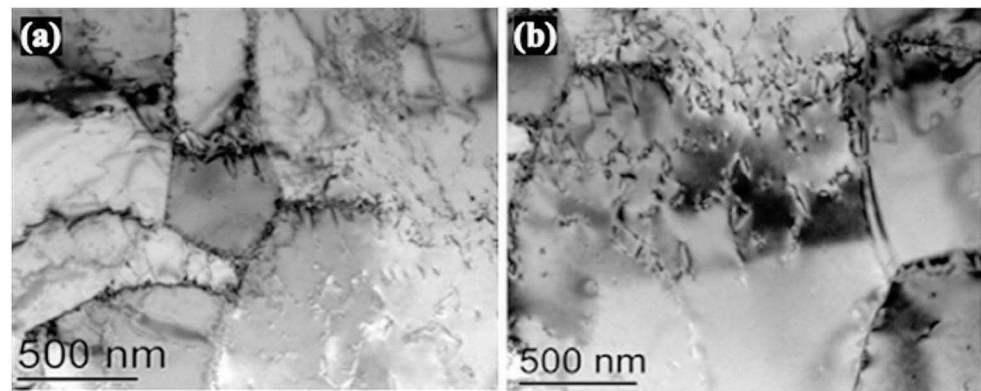


**Fig. 5** TEM images of WCZ shows (a) recrystallization for friction time 4 s and (b) dislocation tangles for friction time 1 s [22]. Reproduced with permission from Elsevier



The presence of HAZ between PM and TMAZ was attributed to: (a) low thermal conductivity of Ti and (b) quenching of welded samples in liquid nitrogen immediately after welding. During LFW, the softened material deforms and gets ejected very rapidly in the form of flash. In this course, the colder base material is continuously fed into TMAZ which subsequently enters the WCZ and exits as flash. There is steep temperature gradient, and material may not get sufficient time to fully recrystallize. Consequently, the grains in the WCZ and TMAZ remain elongated. Only in the case of the highest value of friction time (i.e., 4 s), few refined grains were observed at the boundaries of elongated grains in the WCZ. Furthermore, the temperature and deformation state in the WCZ produce refined grains and large number of tangled and cell dislocations (Fig. 5). The temperature in the TMAZ is found to be lower than beta transus and recrystallization did not occur for a short weld cycle time [22]. The grains in TMAZ and WCZ are elongated because of typical flow of material, which is dragged out from the interface and expelled in the form of flash. In Ti alloy, softened material gets extruded from the interface in (a) the direction of oscillation, and (b) normal to the oscillation. During every stroke, due to friction pressure, the softened

interface material gets expelled along oscillation by shear. The case (b) applies to the material flow during application of forging/upsetting load. Thus, the flow during LFW is directional and the grains get elongated in the direction of flow. Further, the material is constantly fed longitudinally under a constant welding pressure, to compensate the loss of material in the form of flash. The welding cycle is fast and under combined effect of all these factors, the grains remain elongated [21, 22, 49].

The material flow in Cp-Ti is found to be driven from shear and regulated by prismatic slip. The EBSD maps of the LFWed joints reveals anisotropy due to strong texture which was corroborated with the varying microhardness and elastic modulus [22]. The high-speed shear and axial pressure at the interface cause severe plastic deformation (SPD) and the dislocation density increases significantly. The frictional heat results in dynamic recovery simultaneously; leading to redistribution of dislocations in the form of cell and network and dynamic recrystallization (DRX) [22].

Ti-6Al-2Sn-4Zr-2Mo-0.1Si alloy is a near-alpha high strength Ti-alloy, and is denoted as Ti-6242. It also possesses good high temperature strength, resistance to fatigue and corrosion. This alloy finds applications in aerospace,

gas turbine parts and other components that need high strength at elevated temperatures [28, 50]. Such high-end critical products are made by welded joints that work under adverse conditions of stress and temperature. The joints must be free from defect, porosity and voids. The LFWed joints fabricated near metastable beta-transition temperature ( $995 \pm 15$  °C) show a drop in HAZ hardness by 8.6% due to the presence of a large amount of soft metastable  $\beta$  phase. The interfacial material undergoes SPD and DRX especially in the super transus temperature range. The hardness in the WCZ is found to increase to a peak value of  $\sim 399$  HV as compared to 340 HV of PM due to the presence of  $\alpha'$  martensite structure and refined  $\beta$ . The stress relief annealing (SRA) treatment of the welded plate is observed to reduce the average peak hardness of WCZ by 6.5%. On the contrary, HAZ hardness is obtained to recover by 8.6% after SRA due to phase transformation of soft metastable  $\beta$  to  $\alpha$ . The tensile strength of both as-welded and SRA samples gets improved as compared to PM (Fig. 6a) and failure occurs in the PM region. The fatigue behavior of SRA sample, in both low cycle fatigue (LCF) and high cycle fatigue (HCF) regimes, is observed to be similar to that of PM (Fig. 6b) [28]. The LFW of 3D-printed Ti alloys is crucial due to their frequent application in aircraft components. Also, since 3D-printed alloys generally have a hierarchical microstructure composed of cells, melt-pools and large grains, the LFWed microstructure gets significantly varied which is important to understand to explain mechanical properties of the welds. Further studies on LCF and HCF behavior of LFWed Ti alloys are important for the aerospace industry.

## 2.2 LFW of Steels

Among steels, the austenitic stainless steels (ASS) find extensive applications in structural, medical, aerospace, food processing and chemical industries. The ASS AISI316L finds high end applications in aircraft, rapid

railroad transport systems and nuclear power sectors. This ASS has also been reported to involve an increasing welding activity at industrial scale. It possesses low thermal conductivity and high strain hardening and is limited by the reduction in corrosion resistance due to sensitization [51]. The  $\text{Cr}_2\text{O}_3$  and  $\text{Cr}_3\text{C}_2$  formation kinetics is very sensitive to the temperature and time allowed at that temperature, which in turn affects the sensitization. The short LFW cycle time is useful in the welding of ASS and other alloys, which are sensitive to temperature-time kinetics such as age-hardened alloys. In the case of AISI316L, the burn-off rate has a significant influence on the delta-ferrite fraction. A low fraction of delta-ferrite is produced at the high-burn off rate, the highest burn-off rate occurs at mid-range amplitudes and frequencies. The burn-off rate increases almost linearly with increasing welding pressure (Fig. 7) [29].

Medium carbon steel (MCS) has excellent mechanical properties such as high strength, sufficient toughness, better quench hardenability and low cost. It can be hardened, and the surface heat treatment can provide graded properties. The material finds extensive applications in the automobiles, tools and dies [17, 44]. The MCS can be welded successfully at temperatures below lower critical temperature (as shown in Fig. 8a as A1) in the case of 2.6 mm thick MCS alloy. Low frequency and high pressure can produce sound welds at temperatures below A1 line (Fig. 8a), which avoids the formation of brittle martensite. Typically, an axial pressure of 400 MPa and a frequency of 15 Hz produced  $\sim 1.2$  mm wide WCZ that mainly contained equiaxed ferrite and uniformly distributed spheroidal cementite (Fig. 8b) and resulted in a higher impact strength due to the absence of brittle martensite (Fig. 8c). The elongation was observed to increase with increasing welding pressure [30]. Low carbon steel welded by LFW has also shown excellent stress-controlled fatigue results, wherein the joints with higher post-oscillation pressure exhibited a higher fatigue life in comparison to the welds with smaller applied pressure [52]. The applied pressure alters the weld toe shape

**Fig. 6** (a) Tensile strength of as-welded and SRA Ti-6242 LFWed alloy, (b) fatigue life (S-N) curve of LFWed and PM Ti-6242 alloy tested at  $R=0.1$  [28]. Reproduced with permission from MDPI

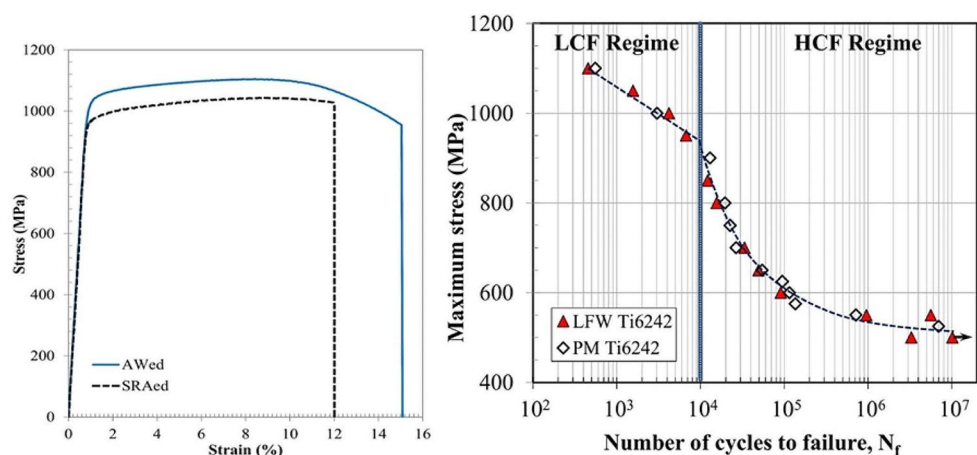


**Fig. 7** Effect of pressure, frequency, and amplitude on burn-off rate in LFW of AISI 316 L [29]. Reproduced with permission from Elsevier

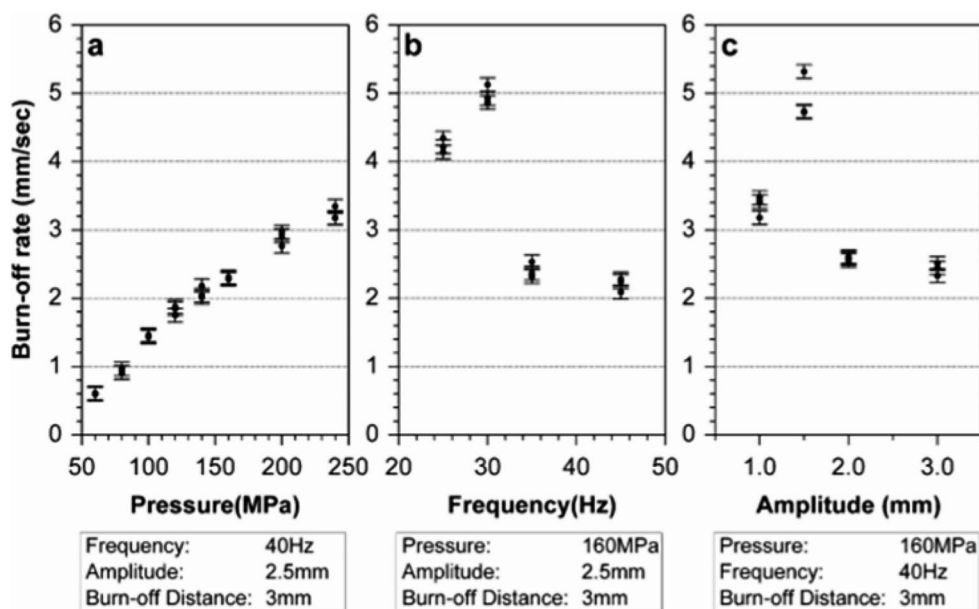
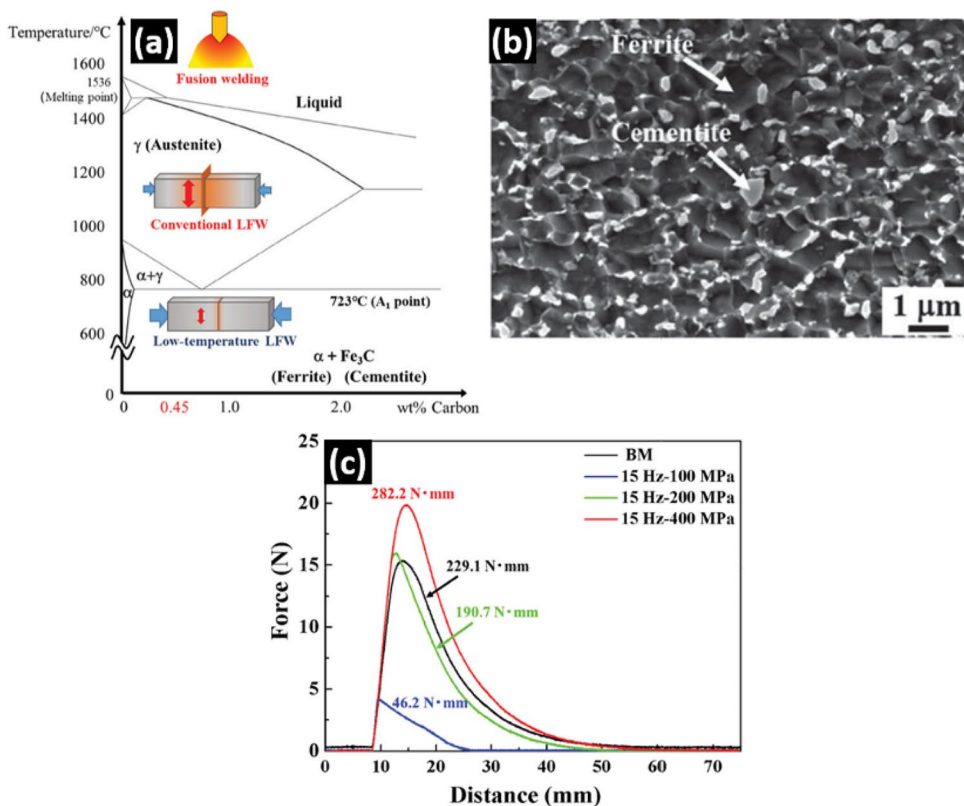


**Fig. 8** Low-temperature LFW of MCS showing (a) welding temperature of different welding processes presented in Fe-C phase diagram, (b) SEM image of martensite free MCS joint, and (c) toughness of LFWed specimens [30]. Reproduced with permission from Sage



which affects the crack propagation under cyclic loading. The weld flash also plays an important role in the fatigue life of LFWed steels [53]. The LFW of steels is expected to have a much wider industrial impact in the upcoming years due to its various advantages over fusion welding techniques and steel's long dominating usage in the manufacturing sectors.

### 2.3 LFW of Aluminum Alloys

Al-alloys require especial consideration for welding, even by conventional arc welding, mainly due to the presence of surface oxide film. Moreover, the welding requirements of bulk and varied shapes in short production cycle leaves very limited alternatives and the LFW fits very well. Welding of a number of Al-alloys such as AA1070 [31], AA7075

[54], AA5052 [32, 55], AA6063 [32, 55] and AA2011 [56, 57] via LFW has been reported in the literature. The lower welding temperatures in LFW enables sound welds with ultrafine grains (UFG). The AA1070 Al-alloy, processed by equal channel angular pressing (ECAP), was welded by LFW at 200 °C in a very short cycle time with a good joint efficiency [58, 59]. The initial ECAPed fine grain structure with an average grain size of  $\sim 1 \mu\text{m}$  resulted in the fine grain size of 1.6–2  $\mu\text{m}$  post welding. A drop in microhardness is generally observed in WCZ of these materials [31].

LFW can efficiently join precipitation-hardened Al-alloys [54–57]. High temperature during welding with a long cycle time risks coarsening and dissolution of strengthening precipitates, which decreases strength. It is reported for AA7075-T651 welds that  $\text{MgZn}_2$  precipitates get dissolved in the TMAZ. However, blocky  $\text{Mg}_3\text{Cr}_2\text{Al}_{18}$  precipitates remained stable in the WCZ and TMAZ [54]. The literature reveals that the size and distribution of these precipitates mainly affect the strength of AA7075 alloy joints [60]. The precipitates in these alloys get coarsened and often dissolved at elevated temperatures and in sufficient times, which significantly reduces the mechanical properties of 7xxx series Al-alloys [61–64]. The softening effect in TMAZ was also observed by Lis et al. (2018) during high-frequency (250 Hz) LFW of AA6063-T5 for the welding time longer than 1 s. Peak temperature of 320 °C was estimated at the weld interface [54]. Temperatures higher than 200 °C starts the softening in these alloys and, full dissolution of the precipitates may take place above 400 °C [65]. The hardness vs. temperature plot at different friction pressure ' $P_{fr}$ ' (Fig. 9a) and different friction time ' $t_{fr}$ ' (Fig. 9b) in AA6063-T5 alloy shows a higher extent of softening with increasing temperature. On the contrary, hardening was observed in TMAZ during LFW of AA5052-O alloy [55].

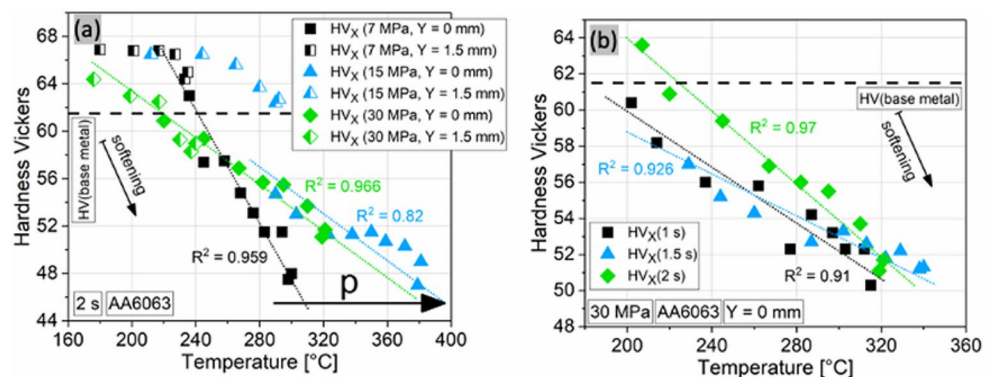
Buffa et al. (2014, 2015) developed numerical models for LFW of AA2011-T3 Al-alloy [56, 57]. The deformation predicted by finite element method (FEM) was compared with actual deformation geometry and the predictions were reported to be fairly accurate. Effective strain value was analyzed and its range for producing sound welds was

determined. Extremely low (1 to 1.12) and maximum values (3.92 to 4.48) of effective strain were calculated for poor and sound welds, respectively [56]. In another study, shear coefficient ratio between shear stress on contact surface and shear yield stress was also determined. The measurements of burn-off, off-load, and in-process torque were used to calculate the contact surface shear stress. The shear yield stress of material was calculated by an integrated experimental/numerical approach. Friction coefficient was calculated as a function of temperature. The developed model was observed to predict the interface temperature [57]. Though FSW is considered as an extremely suitable process for Al alloys, LFW overcomes the limitations of FSW in its ability to join complex shapes, dissimilar geometries, and thick cross-sections. Thus, LFW can play an important role in accelerating the progress in lightweighting goals of the automotive companies.

## 2.4 LFW of Superalloys

The Ni-based superalloys (such as Incoloy, Nimonic alloy, GH4169 superalloys) possess low thermal expansion, excellent high-temperature strength, strong oxidation resistance and high creep resistance in adverse conditions of heat. These alloys are used extensively in the aircraft engine parts such as bladed disks [66–68]. LFW is an exclusive process for the joining requirements of aero-engine parts. LFW has been used to successfully join GH4169. Incomplete extrusion of the softened material or the lack of flash (Fig. 10a–b) leads to inferior joints due to presence of oxides (Fig. 10f). The presence of pores and discontinuity was also observed (Fig. 10f–g). Sufficient flash results in a higher shortening length (more than 4.8 mm) and produced sound joint (Fig. 10c–e). At a higher value of friction time, desirable grain morphology could be produced. A dissolution followed by re-precipitation of carbide-based precipitates was observed at the friction interface at high welding temperatures. The tensile properties of the sound LFWed joints was obtained to be comparable to the base metal (BM) (i.e. 1025 MPa tensile strength and 29.5% elongation)

**Fig. 9** Hardness over effective temperature for AA6063 (a) after  $t_{fr}$ -2 s at different  $P_{fr}$ , and (b) for  $P_{fr}$ -30 MPa after different  $t_{fr}$  [55]. Reproduced with permission from Elsevier





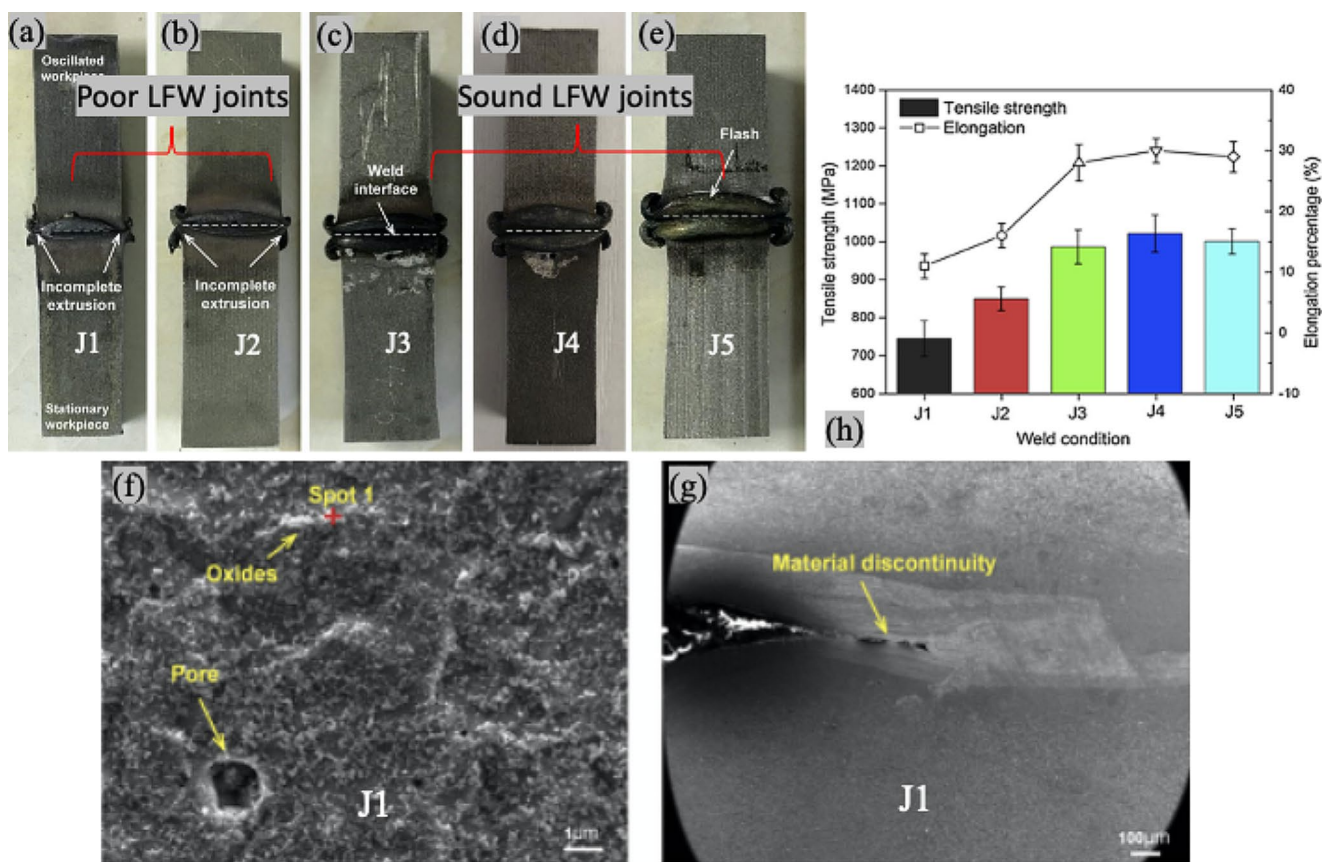


**Fig. 10** LFWed joints welded at (a)  $P_{fr}$ -200 MPa,  $f$ -25 Hz,  $\alpha$ -2.5 mm (J1), (b)  $P_{fr}$ -300 MPa,  $f$ -25 Hz,  $\alpha$ -2.9 mm (J2), (c)  $P_{fr}$ -400 MPa,  $f$ -25 Hz,  $\alpha$ -2.9 mm (J3), (d)  $P_{fr}$ -400 MPa,  $f$ -30 Hz,  $\alpha$ -2.9 mm (J4) (e)  $P_{fr}$ -500 MPa,  $f$ -25 Hz,  $\alpha$ -2.9 mm (J5), (f) SEM image showing pore

and oxide in J1 joint, (g) SEM image showing crack and discontinuity in J1 joint, (h) average tensile strength and % elongation for different joint [33]. Reproduced with permission from Elsevier

(Fig. 10h). This increase was ascribed to the occurrence of DRX. Sufficient DRX takes place in the FIZ, in comparison to TMAZ, which was also confirmed through a greater fraction (~94%) of high-angle grain boundaries (HAGBs) in the FIZ [33]. Due to their application as blisks for aero-engines, the creep behavior of LFWed superalloys is recently being explored. The weld defects such as cracks, pores and inclusions largely impact the creep crack propagation in the LFWed GH4169 superalloy [69]. Nevertheless, a vast and important area concerning the creep behavior of LFWed superalloys remains chiefly unexplored and open to various scientific findings.

The investigation on various types of similar materials and their outcomes have been summarized in Table 1.

The temperature evolved in the WCZ and TMAZ may cause un-favourable phase change in some alloys. During LFW of heat-treatable Al-alloys, coarsening and dissolution of precipitates results in a reduction of joint strength to 70% [21]. Similarly, during welding of carbon steels (especially medium and high carbon steels), the temperature may enter into austenitic range. The short welding causes rapid cooling, and a resultant martensitic transformation may create

brittle phase. In the case of Ti-alloys (such as Ti64) the peak temperature of 1000 °C to 1400 °C in the WCZ has been reported, which is well above the  $\beta$ -transus [44]. However,  $\beta$ -transus temperature is not reached in the TMAZ. The TMAZ microstructure comprises of  $\alpha$ , whereas the WCZ may fully transform to recrystallized  $\beta$ . As the cooling is fast, the recrystallized  $\beta$  transforms to Widmannstetten or martensitic structure. In such, and in similar other cases, the microstructure across the weld becomes highly heterogeneous [44, 45]. Such problems can be tackled by performing LFW at low temperatures (a specially designed low temperature LT-LFW system is available) and post weld heat treatment (PWHT) [21, 44, 46]. The LT-LFW is performed by the control of friction pressure (kept high), oscillation parameters and friction time. These parameters are so controlled that temperature does not exceed the transition value [21]. A lot of work is reported on the PWHT and can be typically referenced from elsewhere [46]. However, the adjustment of welding parameters to minimize the dissolution of strengthening phases seems to be much more effective for LFWed parts, since PWHTs can also cause undesirable changes to the microstructure of base metals.

**Table 1** Summary of linear friction welding of similar materials

S. No.	Workpiece Material	Dimensions	Process Parameters	Remarks	Ref.
1	Pure Titanium	L-50 mm, W- 20 mm, H-10 mm	$f$ -35 Hz - 2.5 mm $P_{fr}$ -50 MPa $t_{fr}$ -0.5~4 s	1. PM Microhardness on-RD-TD (rolling direction-traverse direction) plane-175 HV RD-ND (normal direction) plane-195 HV 2. WCZ microhardness on- RD-TD plane-220 HV RD-ND plane-185 HV 3. Limited continuous dynamic recrystallization in WCZ.	[22]
2	Ti-6Al-2Sn-4Zr-2Mo-0.1Si (Ti6242)	L-33 mm, W- 24.5 mm, H-12 mm	$f$ -50 Hz - 2 mm $P_{fr}$ -90 MPa Burn-off distance-2 mm	1. Microhardness of as-welded sample- PM- 340±7 HV, HAZ- 315±4 HV, WCZ-399±5 HV 2. Microhardness of SRAed sample- PM- 338±5 HV, HAZ- 342±8 HV, WCZ-373±3 HV 3. UTS of as-welded and SRAed samples was-1027±3 MPa and 969±22	[28]
3	Austenitic steel AISI 316 L	L-75 mm, W- 20 mm, H-20 mm	$f$ -25~45 Hz - 1~3 mm $P_{fr}$ -60~240 MPa Burn-off distance- 1~3 mm	1. A strong {111} {112} texture was observed at weld line. 2. Highest burn-off rate occurred at $f$ -30 Hz, A-1.5 mm. 3. High burn-off rate produced less $\delta$ -ferrite fraction. 4. Poor quality welds were produced when all parameters set at low value.	[29]
4	Medium Carbon Steel	L-63 mm, W- 50 mm, H-2.6 mm	$f$ -15~50 Hz - 2 mm $P_{fr}$ -100~400 MPa $t_{fr}$ - 0.85~3.85 s	1. Welding temperature decreased with decreasing $f$ and increasing $P_{fr}$ and low-temperature LFW results. 2. With decreasing $f$ and increasing $P_{fr}$ toughness increases and hardness decreases. 3. At 15 Hz $f$ and 400 MPa $P_{fr}$ sound weld joint was produced that is free from martensite.	[30]
5	Ultrafine grained AA1070	W- 10 mm, H-7 mm	$f$ -36 Hz $P_{fr}$ -30~40 MPa $t_{fr}$ -1.5~2.2 s	1. Average grain growth of 0.6-1 $\mu$ m was observed in WCZ. 2. A small drop of $\sim$ 3-4 HV in microhardness of WCZ was observed. 3. Tensile strength of 83-90% of the PM was observed.	[31]
6	AA7075-T651	W~32 mm, H-6 mm	$f$ -50 Hz $P_{fr}$ -27 MPa $t_{fr}$ -30 s $P_{fg}$ - 83 MPa $t_{fg}$ - 3 s	1. Joint efficiency of 75% due to dissolution of strengthening precipitates. 2. Microhardness of $\sim$ 220 HV was observed at WCZ.	[54]
7	AA6063-T5	W- 11 mm, H- 11 mm	$f$ -250 Hz -1.8 mm $P_{fr}$ -7~30 MPa $t_{fr}$ -0.4~2 s $P_{fg}$ - 151 MPa $t_{fg}$ - 5 s	1. Sound joint was produced at $P_{fr}$ -30 MPa and after $t_{fr}$ - 1 s. 2. Increasing $t_{fr}$ above 1 s causes softening in TMAZ.	[55]
8	AA5052-O	W- 11 mm, H- 11 mm	$f$ -250 Hz -1.8 mm $P_{fr}$ -30 MPa $t_{fr}$ -0.4~2 s $P_{fg}$ - 151 MPa $t_{fg}$ - 5 s	1. Sound joint was produced after $t_{fr}$ - 1.5 s. 2. BM hardness- 60 HV, TMAZ hardness for $t_{fr}$ 0.4, 1, and 1.5s- 75, 67.5, and 64 HV.	[55]
9	AA2011-T3	L-10 mm, W- 10 mm, H-7 mm	$f$ -45 Hz -2 mm $P_{fr}$ -40~80 MPa $t_{fr}$ -1.25 s	1. Sound joint was produced at $P_{fr}$ -60 MPa. 2. Developed numerical model was found efficient to predict the joint geometry.	[56]
10	AA2011-T3	L-10 mm, W- 10 mm, H-7 mm	$f$ -45~71 Hz -2 mm $P_{fr}$ -13~40 MPa $t_{fr}$ -1.5 s	1. At 45 Hz $f$ and 13 MPa $P_{fr}$ combination poor heat generated. 2. Other combination produced sound joints. 3. Developed numerical model was found efficient for weld temperature prediction.	[57]
11	Ni-based GH4169 Super Alloy	L-33 mm, W- 14 mm, H-10 mm	$f$ -25~30 Hz -2.5~2.9 mm, $P_{fr}$ - 200~500 MPa $t_{fr}$ - 5 s	1. Average grain size of BM and WCZ was found $20 \pm 10 \mu$ m and 2-7.5 $\mu$ m, respectively. 2. Hardness of BM, WCZ, and TMAZ was 301, 310-320, and 275-290 HV, respectively. 3. Poor weld produced for two combinations 200 MPa-25 Hz-2.5 mm and 300 MPa-25 Hz-2.9 mm.	[33]

Note L-length, W-width, H-height,  $f$  -frequency,  $\alpha$  - amplitude,  $P_{fr}$  - friction pressure,  $t_{fr}$ -friction time,  $P_{fg}$  - forging pressure,  $t_{fg}$ -forging time

### 3 LFW of Dissimilar Materials

In modular designs, every functional component may be made from different materials to suite the local need of in-service stress/environment conditions. This can bring about huge weight reduction coupled with safe designs. The joining of individual functional components into complete product requires dissimilar materials joining. In most cases the shape, size and material are all usually different. The welding of dissimilar materials is challenging, because of varied properties, and the variations in shape and size add to the problem. It is worthwhile to showcase a structured review of LFW for a variety of materials in dissimilar combinations.

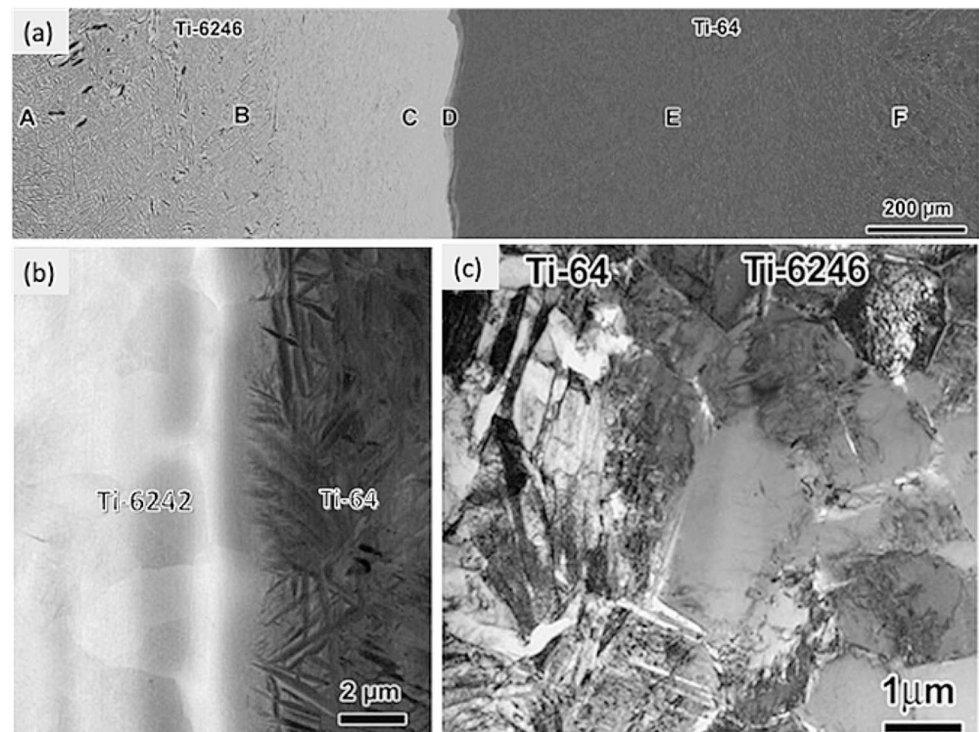
#### 3.1 LFW of Dissimilar Ti-Alloys

The Ti-alloys are characteristically known for high specific strength and magnificent corrosion resistance and superior strength at high temperatures where other light alloys such as Al-alloys, Mg-alloys are not suitable [68, 70, 71]. The Ti-64 ( $\alpha$ - $\beta$  alloy) has lower operational temperature limit ( $\sim 350$  °C) as compared to Ti-6242 (near  $\alpha$  alloy) alloy ( $\sim 510$  °C). The welded joints of these two alloys are particularly useful in fan and compressor rotor of turbo-engines that operates in high load and moderate temperature [71–74]. The microstructure of Ti-6246 contains primary  $\alpha$  and retained  $\beta$  with fine secondary  $\alpha$  inside, whereas the

microstructure of Ti-64 contains equiaxed  $\alpha$  grain and intergranular  $\beta$  [45, 75].

The defect-free LFWed joints between Ti-64 and Ti-6242 dissimilar pair have been successfully made [34, 74] with better interfacial bonding (Fig. 11). A homogeneous single layer flash was formed. Combined thickness of WCZ and TMAZ on both sides of the weld was small ( $\sim 500$   $\mu\text{m}$ ), indicating excellent joint integrity [34]. The WCZ generally consists of recrystallized prior- $\beta$  with  $\alpha'$  martensite in as-welded condition. However, the SRA treatment transforms this structure into acicular  $\alpha + \beta$  structure [34]. Microstructural analysis of LFWed interface between Ti-6242 and Ti-17 (Ti-5Al-2Sn-2Zr-4Mo-4Cr) revealed the formation of cohesive junction. Active migration of grain boundary assisted with continuous DRX (CDRX) was also observed. Fine-grained intermingled structures at the interface sharing both  $\alpha'$  martensite laths (Ti6242 side) and  $\beta$  metastable phase (Ti-17) structures were observed [75]. Fatigue test of the LFWed joint between Ti-64 and Ti-6.5Al-3.5Mo-1.5Zr-0.3Si revealed fatigue life being similar to that of base alloy. The failure location was observed at Ti-64 side far from WCZ [75, 76]. The HCF tests (at  $10^7$  cycles) across LFWed joints between Ti-6242 and Ti64 LF showed a fatigue limit of 450 MPa which is slightly higher than both the base alloys (Fig. 12). Considering the normally large scatter in the fatigue data acquired under dynamic testing, this would indicate that no decrease in the fatigue limit occurred after LFW, suggesting robust bonding achieved between the two dissimilar Ti alloys. Also, fatigue failure in the LCF regime

**Fig. 11** (a) Backscattered electron image showing various zones of welded sample, (b) SEM image of interface of point D as marked in (a), and (c) TEM bright field image of interface [74]. Reproduced with permission from Springer Nature



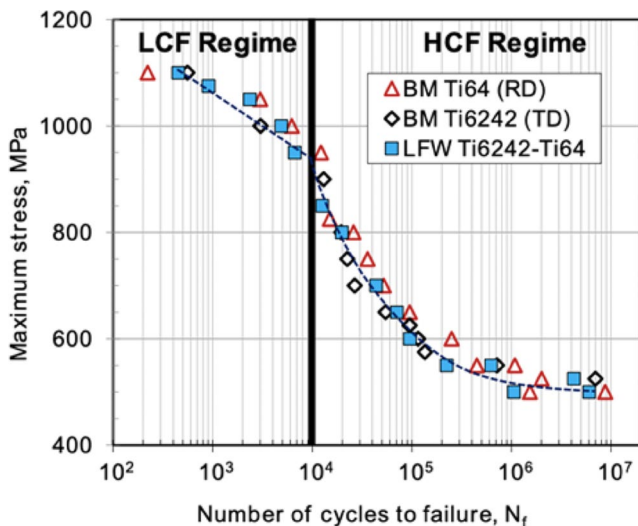


**Fig. 12** Semi-log scale plot of the maximum stress versus the number of cycles to failure ( $N_f$ ) in the LCF and HCF regimes [77]. Reproduced with permission from MDPI

occurred on the Ti-64 side, whereas in the HCF regime it occurred on the Ti6242 side, being  $\sim 3$  mm away from the WCZ [77]. The studies on the cyclic loading behavior of dissimilar LFWed Ti-alloys are therefore promising, which are likely to serve as design solutions for aircraft engineers.

### 3.2 LFW of Stainless Steels with Ti-alloys and Stainless Steels with Superalloys

LFW is distinctive in joining superalloys in diverse combinations and to join superalloys with ferrous materials. The ASS AISI316L has been successfully welded with Zircaloy-4 (Zr-4) by LFW [35]. The Zr-4 is used in nuclear fuel reprocessing plants due to superior corrosion and irradiation resistance, low neutron absorption/capture cross section, etc. The evolution of thermal profiles, peak temperature and interface structure, etc., has been investigated for AISI316L-Zr4 dissimilar LFWed joints. A peak temperature in the range of 922 °C and 956 °C was observed. The interface possessed intimate bonding, free from void and cracks, (Fig. 13a&b). A peak hardness of 250 HV was observed in the intermixed region (Fig. 13c) of welded samples. The XRD confirmed the presence of  $Cr_2Zr$  and  $FeZr_3$  intermetallic particles.

Two different grades of ASSs, which are common in aircraft and aerospace structures, i.e., AISI304 and AISI316 were welded with Ti-64 by LFW. The interface was marked with higher diffusion of Fe, Cr and Ni in Ti. However, the diffusion of Ti and Al in steel was less. The joints with AISI316 produced intermetallic compounds (IMCs) which caused failure at the interface. Both the dissimilar joints were found to possess a similar microstructure on the ASS side of the interface. The deformed grains in TMAZ were

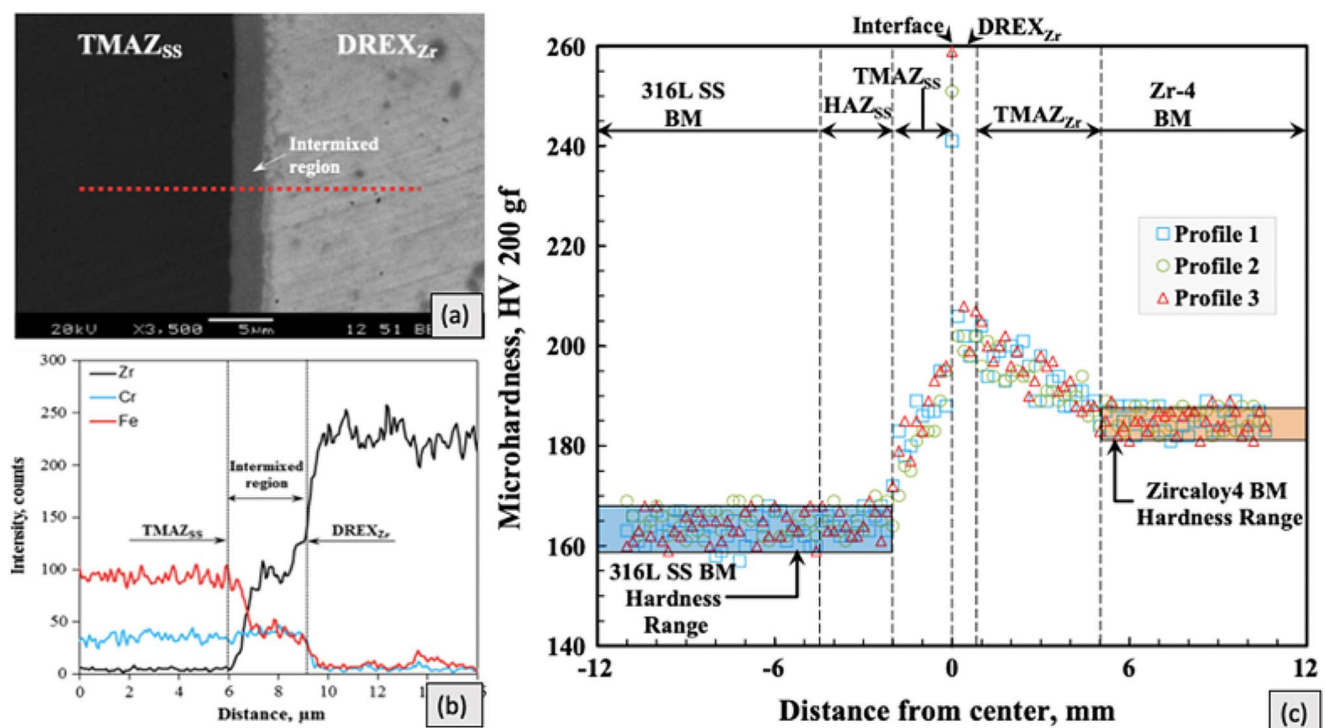


**Fig. 13** (a) BSE-SEM image of joints, (b) SEM-EDS line scan detecting presence of major elements, and (c) microhardness profile [35]. Reproduced with permission from Springer Nature

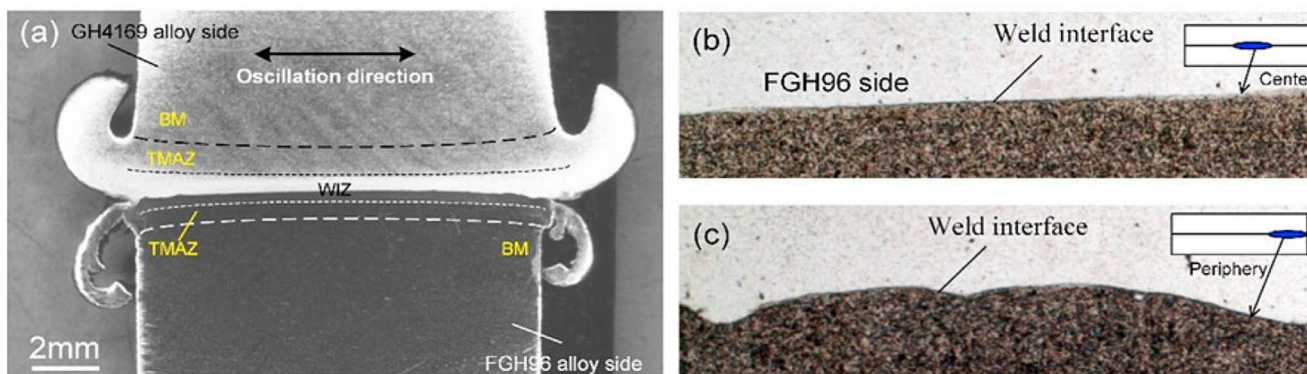


**Fig. 14** (a) Macro-image of linear friction welded joint of FGH4096/GH4169 superalloys, and (b) & (c) weld interface at different locations of the joint [36]. Reproduced with permission from Elsevier

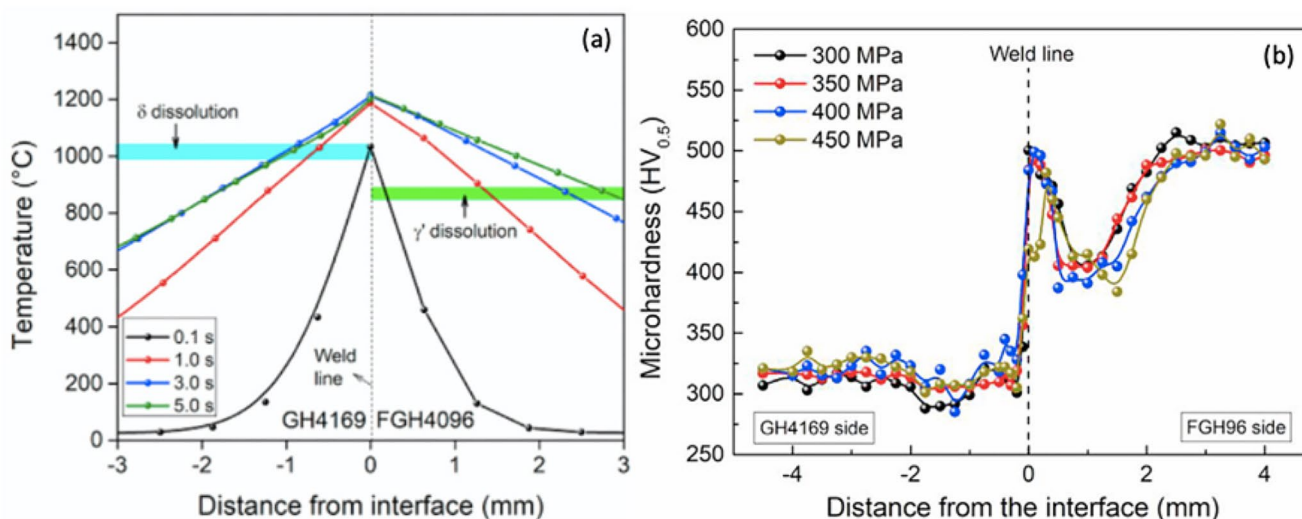


**Fig. 15** (a) Distribution of temperature across the interface for friction time of 0.1 s to 5 s, and (b) microhardness profile for different value of friction pressure [36]. Reproduced with permission from Elsevier

found to extend up to 250  $\mu\text{m}$  adjacent to the fine grain region in the ASS side. Unlike ASS side, the microstructure was complex on the Ti-64 side. The Ti side microstructure between interface to base material (i.e., in TMAZ of Ti-64 side) was observed to consist of: (a) predominant beta region, (b) martensitic zone and (c) deformed grain zone. Significant diffusion of Fe and Cr was found in the predominant beta zone, mainly because both the elements are beta stabilizers. The findings demonstrated that the IMCs were not present in the AISI304, but were present in the AISI316 joint in significant amount; which also resulted in the formation of micro-crack near the interface [78]. Although LFW involves a shorter thermal cycle with smaller peak temperatures, the formation of IMCs cannot be avoided completely, which can lead to detrimental effect on the weld properties. However, the nature of these IMCs is can be different due to relatively smaller temperatures and non-equilibrium conditions during LFW.

### 3.3 LFW of Dissimilar Superalloys

A combination of Ni-based superalloys, i.e., FGH4096 and GH4169 (US Inconel 718) is used in aircraft engine parts such as BLISK (Disk + Blade = BLISK). The BLISK is majorly manufactured by LFW. The LFW of this dissimilar superalloy pair was marked with tightly curled flash which was mostly defect free. The flash on the GH side was significantly thicker than the flash on the FGH side [36]. This indicates that the amount of deformation was higher in GH than FGH (Fig. 14a). Defect-free interface (Fig. 14b, c) and significant grain refinement were observed in the WCZ. The widths of plasticized zones were measured as 1.6 mm and 2.05 mm on the FGH and GH sides, respectively [36].

The WCZ microstructure was refined due to DRX, and dissolution of precipitates ( $\delta$  phase in GH4169 and  $\gamma'$  in FGH4096) as shown in Fig. 15a&b) occurred due to the high temperature of  $\sim 1230^\circ\text{C}$  in WCZ. While the peak

temperature increased significantly with increase in the friction time from 0.1 s to 1 s, relatively smaller temperature increments were observed for the friction time of 1–5 s, as shown in Fig. 15a. Partial dissolution of precipitates occurred in the TMAZ due to lower temperatures. The values of hardness in WCZ (Fig. 15b) were found to be comparable to that of FGH4096 base alloy [79]. Also, a relatively smaller variation was observed across the weld zones in the microhardness of GH4169 alloy as compared to FGH4096 alloy. The partial dissolution of strengthening phases and incomplete DRX resulted in a decrease in hardness in the TMAZ. For the dissimilar LFW of the IN718 and FGH96 superalloys, enhanced dissolution of  $\gamma'$  phase in FGH96 and  $\delta$  phase in IN718 was also observed from TMAZ to the interface [80]. Though discontinuous DRX remained dominant, increase in continuous DRX was observed with increasing oscillation frequency or drop in applied pressure.

### 3.4 LFW of Dissimilar Aluminum Alloys

Investigations involving LFW have been reported for joining dissimilar Al-alloys (e.g., AA6082-T6 to AA2011-T8) in different geometries at the interface [37]. Among these two alloys, AA2011 generally shows a larger flow stress at room temperature as well as at elevated temperature ( $\sim 200$ – $450$  °C). The effects of frequency and pressure (within parameter window as shown in Fig. 16a–b) for AA2011-AA6082 and AA6082-AA2011 have been reported. A combination of low frequency and low pressure did not produce joining due to insufficient heat. Increasing the values of parameters resulted in the increase in the heat input and sound joint was produced. But with further increase in parameter values, the specimens could not bear the applied pressure and collapsed. It was suggested that the material with higher flow stress/hardness preferably be made smaller and vice-versa [37]. For the LFW of AA5052/AA6061 dissimilar pair, the high applied pressure of 200 MPa resulted in a tensile strength similar to that of the AA5052 base metal, due to increase in the density of low angle grain boundaries [81]. Thus, the successful LFW of dissimilar Al-alloys

is expected to encourage the fabrication of tailor-welded blanks for application in automobiles and airplanes.

### 3.5 LFW of Aluminum Alloys to Other Materials

The welding of Al-alloys with other materials gives a common interface such as with Ti-alloys, stainless steel and between different Al-alloys, which is often required in aircraft and aerospace. Similarly, Al-Cu interfaces are common in heat exchanger and electrical appliances. Investigations on LFW of aluminum in dissimilar alloy pair (as shown in Fig. 17) with Cu [38], Mg [39], stainless steel [40, 82] and metal matrix composites [41] have been reported. A comparison based on the ratio of conductivity to density of Al is twice more beneficial than copper. Aluminum is, therefore, considered as an important material when design factor is concerned. The Al and Cu are used in overhead transmission lines, in which case, the resistivity becomes an important response. The LFWed joints are found to possess very low electrical resistivity due to  $\text{CuAl}_2$  IMCs present as thin layers ( $< 1$   $\mu\text{m}$ ) or as discontinuous particles. Apart from  $\text{CuAl}_2$  IMCs, a large amount of Cu particles is also observed on the Al side as shown in Fig. 17a [38].

Al and Mg dissimilar joint is a prominent dissimilar pair for applications in automobile and aviation sectors. However, the Al-Mg dissimilar welding is challenging due to low temperature ( $437$  to  $450$  °C) eutectic reaction forming IMCs [83], which causes hot cracking at the joint interface. The  $\text{Al}_{12}\text{Mg}_{17}$  and  $\text{Al}_3\text{Mg}_2$  IMCs are formed during LFW between AA6082-T6 and AZ31 (Fig. 17b). Interestingly, the volume fraction of IMCs is observed to decrease with increasing applied pressure mainly because (a) the increased pressure results in expulsion of a large amount of flash, (b) the cycle time of LFWed joint is very short, and (c) it lowers the welding temperature. Consequently, the pressure is kept high (the values are mentioned in Table 2) in order to obtain sound joint [39].

During the high-frequency LFW between AA5083 and AISI304, the thickness of IMC layer was found to decrease from 1 to 2  $\mu\text{m}$  to 500 nm with increasing pressure, which

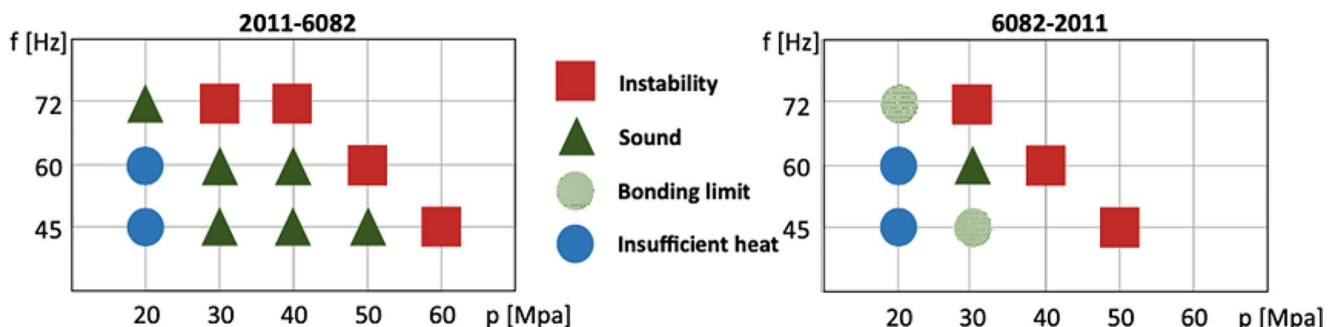
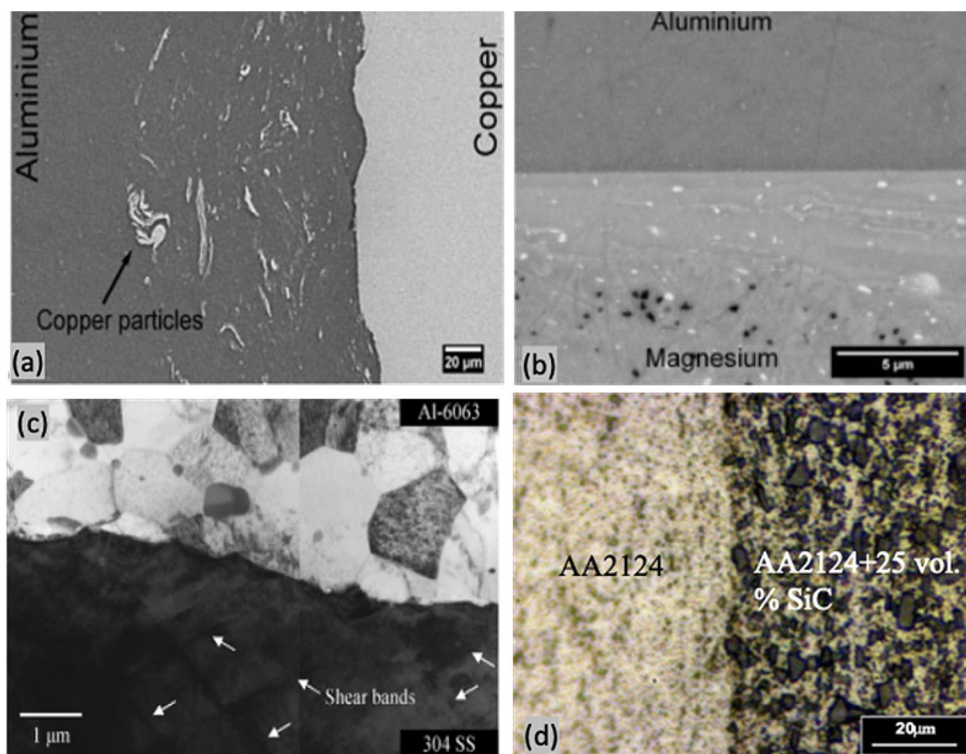


Fig. 16 Process parameter window at varying frequency and interface pressure for (a) AA2011-AA6082 and, (b) AA6082-AA2011 joint configurations [37]. Reproduced with permission from Springer Nature

**Fig. 17** Micrographs showing WCZ of LFWed interface of (a) Al-Cu, (b) Al-Mg, (c) Al-SS, and (d) Al-AMMC joints [38–41]. Reproduced with permission from Elsevier and Sage



resulted in improved joint efficiency. It is found that an increase in friction time results in the localized growth of the IMC layer and, a further increase results in the cracking, tearing, and separation of the IMC layer. All these factors consequently lower the joint strength (Fig. 18) [40]. In the case of Si bearing 6xxx series Al-alloys, the Si hinders the formation of IMC and generally results in no or very thin IMC layer in comparison to 5xxx series alloys. This is confirmed through LFW between AA6063 and AISI304, in which a very thin layer of IMC (<50 nm in thickness) was observed. Figure 17c shows an image of this joint indicating shear bands depicting plastic deformation. However, being heat-treatable Al alloy, its interfacial structure and properties can be severely affected due to softening at high temperatures, which prevails at high frequency and friction time [40].

The joining of AA2124 with 25 vol% SiC-Al metal matrix composite (AMMC) has also been performed via LFW. The AMMCs enhance various properties such as specific stiffness and strength, wear resistance and thermal stability, while regulating the isotropy. These composites find applications in aerospace and automobiles, rapid transport systems, electronic substrates, and packaging machines, etc. [41]. The welding of AMMC and AA2024 by LFW can produce defect free joints (Fig. 17d). Uniform particle distribution in the AMMC side has been confirmed through microstructural analysis. It was also found that the tensile properties of the joints were not much affected with the

change in welding parameters. However, the extent of material flow was comparatively low on the AMMC side due to its higher hardness [41]. The welding of Al alloys with high-melting and high strength materials is generally challenging due to significant disparity in thermophysical properties. However, the observable success of LFW in this area may lead to numerous application-oriented welds suited to increase the functionality of engineered parts.

## 4 Concluding Summary

Conventional fusion welding relies on phase equilibrium-based joint solidification which limits the weldability of a large number of dissimilar materials. Solid-state welding enables the joining of metallurgically non-compatible materials. Whereas most solid-state welding routes have shape and size limitations, the linear friction welding has a distinction of ability to join without such restrictions. The weld cycle time is also very short.

Linear friction welding can successfully join Ti and its alloys, steels and stainless steels, Al-alloys and Ni-based super alloy, etc. LFW is has also demonstrated dissimilar material joining in material pairs including Ti alloys (i.e., Ti-6Al-4 V and Ti-6Al-2Sn-4Zr-2Mo-0.1Si), AISI316L and Zircaloy-4, FGH4096 and GH4169 superalloys, dissimilar Al-alloys, AA1050 to Copper, AA6082-T6 to AZ31, Al-alloy to stainless steel, Al-alloy to composites, and IN718

**Table 2** Summary of linear friction welding of dissimilar alloys

S. No.	Materials		Dimensions	Process Parameters	Remarks	Ref.
	A	B				
1.	Ti-6Al-4 V (Ti-64)	Ti-6Al-2Sn-4Zr-2Mo-0.1Si (Ti-6242)	L-33 mm, W-24.5 mm, H-12 mm	$f$ - 50 Hz -2 mm $\Phi_{fr}$ -90 MPa Burn-off distance-2 mm	1. Enhancement of 22% and 7% in microhardness was observed in WCZ of as-welded and SRAed weld joint, respectively. 2. $\sim$ 12% and $\sim$ 8% improvement in UTS was observed in as-welded and SRAed weld plate, respectively, as compared to BM.	[34]
2.	Ti-64	Ti-6242	L-33 mm, W-24.5 mm, H-12 mm	$f$ - 50 Hz -2 mm $\Phi_{fr}$ -90 MPa $P_{fg}$ -90 MPa Burn-off distance-2 mm $t_{fr} + t_{fg} \sim 1.3$ s	1. 0.6 mm wide HAZ was observed at both sides. 2. A drop of $\sim$ 4% and $\sim$ 3% in HAZ hardness was found in Ti-6242 and Ti-64 sides, respectively. 3. Highest hardness observed at WCZ due to formation $\alpha'$ martensite within $\beta$ grained structure. 4. Improvement in tensile properties and fatigue performance was observed.	[77]
3.	316 L Stainless Steel	Zircaloy-4 (Zr-4)	L-35 mm, W-26 mm, H-12 mm	$f$ - 100 Hz -2 mm $\Phi_{fr}$ -90 MPa Pressure at Conditioning phase-70 MPa Burn off phase-100 MPa Forging Phase-150 MPa	1. Yield Strength- $316 \pm 9$ MPa, Tensile Strength- $418 \pm 14$ MPa, and %Elongation- $2.1 \pm 0.1$ %. 2. Good fatigue resistance was observed with a fatigue limit of 325 MPa.	[35]
4.	FGH4096 super-alloy	GH4169 super-alloy	L-33 mm, W 14 mm, H-10 mm	$f$ -25 Hz -2.9 mm $\Phi_{fr}$ -300~450 MPa $t_{fr}$ -5 s	1. Hardness of TMAZ of both side decreased due to partial dissolution of strengthening precipitates. 2. DRX and Hall-Petch strengthening at WCZ resulted in improved hardness. 3. $\sim$ 3.7 mm wide WCZ was observed.	[36]
5.	AISI304	EN-8	14 mm $\times$ 6 mm $\times$ 65 mm in size	$f$ -22 Hz -2.4 mm $\Phi_{fr}$ -185~200 MPa $t_{fr}$ -10~60 s	1. TMAZ marked with deformed and elongated structure. 2. 16% higher grain size in SS and 26% in EN-8 sides of HAZ were observed. 3. Average microhardness in SS and EN-8 sides were found to 207.95 and 276.73 HV respectively. The hardness increased from TMAZ to weld centre and hardness peak of 738.8 HV was found at the WCZ	[84]
6.	AA2011-T8	AA6082-T6	Dissimilar Cross-section: 10 mm $\times$ 10 mm $\times$ 10 mm and 10 mm $\times$ 10 mm $\times$ 7 mm	$f$ -45~72 Hz -3 mm $\Phi_{fr}$ - 20~60 MPa $t_{fr}$ - 2.25 s	1. At 60 Hz frequency and 30 MPa interface pressure, the observed avg. grain size of WCZ, TMAZ, and HAZ for 2011-6082 joint configuration was 5.9, 18.4 and 33.7 $\mu$ m. 2. Grain refinement could not be observed for 6082-2011 welded at 45 Hz and 30 MPa due to no DRX. 3. Hardness at the WCZ reduced due to softening of strengthening precipitates.	[37]
7.	AA1050	Copper (C101)	L-50 mm, W-50 mm, H-12 mm	$f$ -50 Hz -1.4~2 mm $\Phi_{fr}$ -50~75 MPa $t_{fr}$ -1.5 s $P_{fg}$ -75 MPa $t_{fg}$ -5 s Burn-off distance-1~2 mm	1. Weld joint showed good tensile and bend properties. 2. Hardness enhancement was observed at the WCZ. 3. Electrical resistivity test of the interface revealed good electrical properties.	[38]



Table 2 (continued)

S. No.	Materials		Dimensions	Process Parameters	Remarks	Ref.
	A	B				
8.	AA 6082-T6	AZ31	L-50 mm, W-12 mm	$f$ -25~50 Hz $\alpha$ -1~3 mm $P_{fr}$ -40~133 MPa $P_{fg}$ -100~133 MPa Burn-off distance-2 mm Sliding Velocity-157~785 mm/sec	1. All weld depicts lower UTS as compared to BM and failed from the interface. 2. Poor repeatability in weld properties was observed. 3. High sliding velocities found detrimental in producing good welds. 4. Intermetallic phases of $Al_{12}Mg_{17}$ and $Al_3Mg_2$ were detected at the weld interface.	[39]
9.	AA5083-O	SS 304	L-35 mm, W-35 mm, H-10 mm	$f$ -245 Hz $\alpha$ -1.8 mm Friction Load- 7.2~14.3 kN $t_{fr}$ -0.5~6 s Forging Load-22 kN $t_{fg}$ -5 s	1. Joint efficiency- 94.9% at high value of friction pressure and 1 s $t_{fr}$ . 2. IMC layer was found to be affected by friction pressure. Minimum thickness of IMC layer observed was 500 nm.	[40]
10.	AA6063-T5	SS 304		$f$ -245 Hz $\alpha$ -1.8 mm Friction Load- 4.6~10.7 kN $t_{fr}$ -0.2~6 s Forging Load-22 kN $t_{fg}$ -5 s	1. Joint efficiency- 89.7% at mid value of friction pressure and 1 s $t_{fr}$ . 2. Thin IMC layer of <50 nm was observed.	[40]
11.	AA2024	AA2124 + 25Vol.% SiC <sub>p</sub>	L-36 mm, W-36 mm, H-15 mm	$f$ -50 Hz $\alpha$ -2 mm $P_{fr}$ -130~185 MPa Forging force- 70~100 KN Burn-off distance-2 mm	1. Joint efficiency-~90%. 2. Fatigue strength of 190 MPa was observed at $10^7$ cycles. 3. Lower hardness was observed at WCZ due to softening/ dissolution of strengthening precipitates.	[41]

Note L-length, W-width, H-height,  $f$ -frequency,  $\alpha$ -amplitude,  $P_{fr}$ - friction pressure,  $t_{fr}$ -friction time,  $P_{fg}$ - forging pressure,  $t_{fg}$ -forging time

to Ti6Al4V, etc. The effects of frequency and amplitude of oscillation, friction pressure, forge pressure and burn-off distance, etc., have been mainly investigated. The empirical relationship to estimate heat input during LFW is established as a function of friction pressure, amplitude and frequency of oscillation.

Typical LFWed joints possess characteristic microstructural zones, namely weld centre zone (WCZ), thermo-mechanically affected zone (TMAZ) and heat-affected zone (HAZ). Grains in WCZ generally are fine yet elongated, the grains in TMAZ are also elongated and HAZ consists of coarser grains. The materials and components that are joined by LFW find major applications in promising sectors such as space, aerospace, aircraft, and rapid transportation. The strategic nature of products, size and shape, and component's material makes it very important. A structured summary as drawn out from the reported literature is given as follows.

## 4.1 Linear Friction Welding of some Important Materials

The parts having similar or dissimilar shape and size joined by LFW are used in a number of important applications. Typical examples include turbine blade joined to disc (BLISK), age-hardened Al-alloy ribs of aircraft wings, Ti-tabs joined to rocket fuel tanks, etc. The LFW is flexible to accommodate sizes ranging from as small as less than a kilogram to several tonnes.

### 4.1.1 LFW of Titanium and its Alloys

The LFW welds for Ti, due to its low thermal conductivity, completes in a very small cycle time ranging from 0.5 s to 4 s. The Ti WCZ possesses ultrafine grains. Temperature in TMAZ is found to be below  $\beta$  transus and recrystallization is not complete due to short weld cycle time. The EBSD maps of the Cp-Ti LFWed joints reveal strong texture. The temperature in near  $\alpha$ -Ti-6Al-2Sn-4Zr-2Mo-0.1Si can reach to near metastable  $\beta$ -transus range (about  $995 \pm 15$  °C). The interface material experiences severe plastic deformation at high temperature during LFW. This results in dynamic

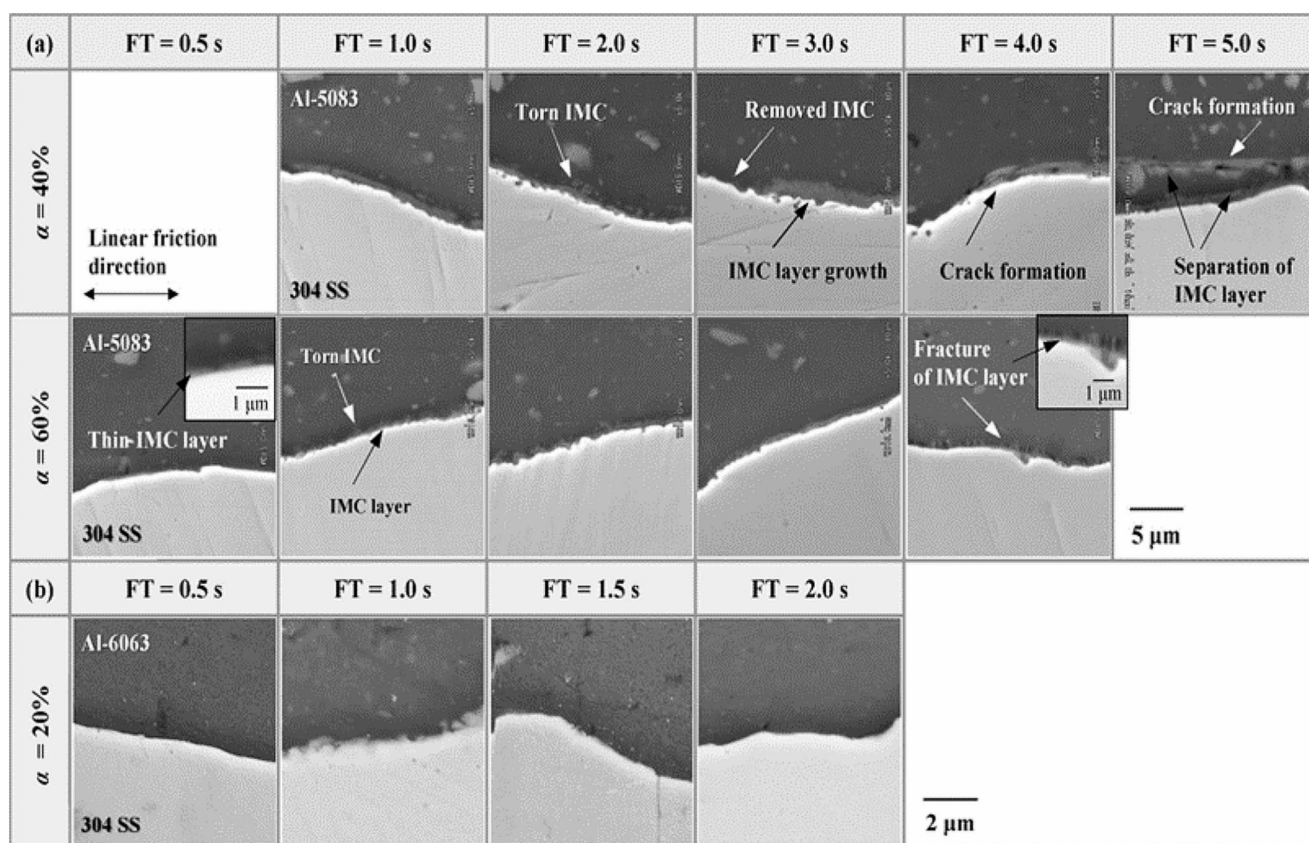


**Fig. 18** SEM images showing effect of friction time (FT) and friction pressure on the formation of IMC layer during LFW of (a) AA5083-AISI304 and (b) AA6063/AISI304 joints [40]. Reproduced with permission from Elsevier

recrystallization (DRX) especially in the super transus temperature range which reaches in the WCZ and results in increase in hardness with average peak of  $\sim 399$  HV as compared to 340 HV of base alloy. Stress relieve annealing treatment of welded plate decreases the average peak hardness of WCZ.

#### 4.1.2 LFW of Steels

Stainless steels possess low thermal conductivity, high strain hardening and are limited by reduction in corrosion resistance due to sensitization during welding. The sensitization is alleviated due to short cycle time, though. In austenitic stainless steels high-burn off rate reduces delta-ferrite fraction. Medium carbon steel can be welded successfully at temperatures below lower critical temperature. Low frequency and high applied pressure can produce sound welds. Typically, 400 MPa friction pressure and 15 Hz frequency produced  $\sim 1.2$  mm wide WCZ.

#### 4.1.3 LFW of Aluminum Alloys

Welding of a number of Al-alloys such as AA1070, AA7075, AA5052, AA6063 and AA2011 by LFW has been

done successfully, as welding can be done at about 200 °C. During welding of age-hardened Al-alloys dissolution of  $MgZn_2$  precipitate was evident in the TMAZ. Greater softening and fracture location were also observed in TMAZ. However, blocky  $Mg_3Cr_2Al_{18}$  precipitate did not dissolve in the WCZ and TMAZ.

#### 4.1.4 LFW of Superalloys

The traditional joining of turbo-engine blade has evolved from the fastening to laser welding and now the LFW is an exclusive process. During LFW of superalloys (typically in the case of GH4169), high friction time results in evolution of desirable grain morphology. A dissolution followed by re-precipitation of carbide precipitates can occur at the interface at high welding temperature. The microhardness is found to decrease from the friction interface zone to TMAZ followed by a sharp rise in the BM. The tensile strength of the sound LFWed joints was even reported to be somewhat higher than that of base material (which was probably related to the experimental scatter).

#### 4.1.5 LFW between Dissimilar Ti-alloys

The Ti-64 ( $\alpha$ - $\beta$  alloy) products have lower operational temperature limit ( $\sim 350^\circ\text{C}$ ) as compared to Ti-6242 (near  $\alpha$  alloy) alloy ( $\sim 510^\circ\text{C}$ ). The welded joints of these two alloys are useful in fan and compressor rotor of turbo-engines. The microstructure of Ti-6246 contains primary  $\alpha$  and retained  $\beta$  with fine secondary  $\alpha$  inside. Whereas the microstructure of Ti-64 contains equiaxed  $\alpha$  grain and inter-granular  $\beta$ . The LFWed joints formed between Ti-64 and Ti-6242 are free from defects and show homogeneous single layer flash formation. Combined thickness of WCZ and TMAZ on both sides of the weld was small ( $\sim 500\ \mu\text{m}$ ), indicating excellent joint integrity. WCZ of joint between these alloys consists of recrystallized prior- $\beta$  grains with  $\alpha'$  martensite. The SRA treatment of joints transforms this structure in to acicular  $\alpha + \beta$  structure.

#### 4.1.6 LFW between Superalloys and Stainless Steels

Peak interface temperature in the range of  $922$  and  $956^\circ\text{C}$  is evolved during LFW between stainless steel and Zircaloy-4 (Zr-4). The intermixed regions have the presence of  $\text{Cr}_2\text{Zr}$  and  $\text{FeZr}_3$  intermetallic particles. During LFW between FGH4096 and GH4169 the flash on the GH side was significantly thicker than that on the FGH side. Significant grain refinement occurs in WCZ and the size of plasticized zones is small (typically about  $1.6\ \text{mm}$  and  $2.05\ \text{mm}$  on the FGH4069 and GH4169 sides, respectively). The strengthening precipitates ( $\delta$  phase in GH4169 and  $\gamma'$  in FGH4069) get dissolved in WCZ at a high temperature of  $\sim 1230^\circ\text{C}$  which evolved at the interface.

#### 4.1.7 LFW between Aluminum Alloys

The successful LFW between AA6082-T6 to AA2011-T8 with different geometries at the contacting surface has been performed with adequate heat input. At low frequency and friction pressure the joining did not occur due to insufficient heat input, while the high heat input may cause the specimens to collapse due to softening. LFW between Al-alloys and Cu, Mg, stainless steel or metal matrix composites has been reported. The LFWed joints are found to possess good electrical conductivity. The evolution of  $\text{CuAl}_2$  intermetallic compound in thin layers (typically  $< 1\ \mu\text{m}$ ) contributes to enhanced conductivity. During LFW between Al and Mg alloys, the eutectic phase-  $\text{Al}_{12}\text{Mg}_{17}$  and  $\text{Al}_3\text{Mg}_2$  IMCs lead to hot-cracking.

During high frequency LFW between AA5083 and AISI304, the IMC layer thickness was found to reduce with increasing friction pressure which improved the joint efficiency. An increase in friction time causes a thicker IMC

layer. Further increase results in cracking and separation of the IMC layer. The Si 6xxx series in Al-alloys hinders the formation of IMC in comparison to 5xxx series of Al alloys. Welding between age-hardened AA2124 and 25 vol% SiC-Aluminum metals matrix composite has been performed by LFW. The material flow during welding between this material pair is comparatively low on the composite side due to its higher hardness.

**Author Contributions** All authors contributed equally to this work.

**Funding** No funding was received for this work.

#### Declarations

**Conflict of Interest** Authors declare no conflict of interest.

#### References

1. E. Akca, A. Gürsel, *Period. Eng. Nat. Sci.* **4**, 1–8 (2016). <https://doi.org/10.21533/pen.v4i1.46>
2. A.M. Abed, S.A. Jasim, M.M.A. Lashin, M.N. Rodin, M.Z. Mahmoud, M.H. Ali, I. Husein, M.M. Kadhim, A.H. Abdulkadhim, L. Thangavelu, Y.F. Mustafa, A.H. Jabbar, *Mater. Today Commun.* **31**, 103471 (2022). <https://doi.org/10.1016/j.mtcomm.2022.103471>
3. M. Eizadjou, H. Danesh Manesh, K. Janghorban, *Mater. Des.* **29**, 909–913 (2008). <https://doi.org/10.1016/j.matdes.2007.03.020>
4. C. Egger, M. Kroll, K. Kern, Y. Steimer, M. Schreiner, W. Tillmann, *Materials* **15**, 3615 (2022). <https://doi.org/10.3390/ma15103615>
5. M. Samiuddin, J. Li, X. Sun, J. Xiong, *Metall. Res. Technol.* **119**, 312 (2022). <https://doi.org/10.1051/metal/2022019>
6. H. Yamagishi, *Metall. Mater. Trans. A* **53**, 264–276 (2022). <https://doi.org/10.1007/s11661-021-06518-9>
7. Y. Ou, Y. Deng, W. Zhang, Y. Zhao, J. Zeng, *Proc. Inst. Mech. Eng. Pt. L J. Mater. Des. Appl.* **237**, 437–450 (2023). <https://doi.org/10.1177/14644207221117671>
8. N.F. Lone, N. Ali, M.H. Abidi, D. Bajaj, T. Khan, D. Chen, A. Al-Ahmari, A.N. Siddiquee, *Int. J. Adv. Manuf. Tech.* **131**, 5305–5323 (2024). <https://doi.org/10.1007/s00170-024-13352-x>
9. F.A. Hashmi, H.B. Mohamed Ali, N.F. Lone, R. Azma, A.N. Siddiquee, M. Ashraf Mir, T. Ahmad, F.A. Mir, *Adv. Mater. Process. Technol.* **9**, 169–185 (2023). <https://doi.org/10.1080/2374068X.2022.2088112>
10. J. Wang, X. Li, H. Yan, X. Wang, Y. Wang, *Int. J. Adv. Manuf. Tech.* **122**, 3595–3606 (2022). <https://doi.org/10.1007/s00170-022-10102-9>
11. U. Khan, N.Z. Khan, J. Gulati, *Procedia Eng.* **173**, 1447–1454 (2017). <https://doi.org/10.1016/j.proeng.2016.12.210>
12. B. Skowrońska, M. Bober, P. Kołodziejczak, M. Baranowski, M. Kozłowski, T. Chmielewski, *Appl. Sci.* **12**, 9034 (2022). <https://doi.org/10.3390/app12189034>
13. K. Zhang, X. Qian, J. Chen, J. Chen, H. Lu, *Mater. Des.* **224**, 111400 (2022). <https://doi.org/10.1016/j.matdes.2022.111400>
14. B. Hinze, in *Superalloys 2020: Proceedings of the 14th International Symposium on Superalloys*, ed. by S. Tin, M. Hardy, J. Clews, J. Cormier, Q. Feng, J. Marcin, C. O'Brien, A. Suzuki. Virtual, 13–16 September 2021 (Springer, Cham, 2020), pp. 365–373. [https://doi.org/10.1007/978-3-030-51834-9\\_35](https://doi.org/10.1007/978-3-030-51834-9_35)

15. S. Tabaie, F. Rézai-Aria, B.C.D. Flipo, M. Jahazi, J. Mater. Sci. Technol. **96**, 248–261 (2022). <https://doi.org/10.1016/j.jmst.2021.03.086>
16. P. Zhao, Y. Tao, K. Fang, M. Guo, Q. Chu, J. Tao, Q. Yuan, Y. Li, Mater. Sci. Eng. A **854**, 143880 (2022). <https://doi.org/10.1016/j.msea.2022.143880>
17. J.-W. Choi, Y. Aoki, K. Ushioda, H. Fujii, J. Manuf. Process. **75**, 651–663 (2022). <https://doi.org/10.1016/j.jmapro.2022.01.033>
18. J.-W. Choi, W. Li, K. Ushioda, M. Yamamoto, H. Fujii, Sci. Technol. Weld. Join. **27**, 92–102 (2022). <https://doi.org/10.1080/13621718.2021.2013710>
19. A. Vairis, M. Frost, Mater. Manuf. Process. **21**, 766–773 (2006). <https://doi.org/10.1080/03602550600728356>
20. J.W. Choi, Y. Aoki, K. Ushioda, H. Fujii, Scr. Mater. **191**, 12–16 (2021). <https://doi.org/10.1016/j.scriptamat.2020.09.013>
21. Y. Aoki, R. Kuroiwa, H. Fujii, G. Murayama, M. Yasuyama, ISIJ Int. **59**, 1853–1859 (2019). <https://doi.org/10.2355/isijinternational.ISIJINT-2018-458>
22. X.Y. Wang, W.Y. Li, T.J. Ma, A. Vairis, Mater. Des. **116**, 115–126 (2017). <https://doi.org/10.1016/j.matdes.2016.12.005>
23. F. Khan, T. Miura, T. Ito, Y. Morisada, K. Ushioda, H. Fujii, J. Manuf. Process. **109**, 512–523 (2024). <https://doi.org/10.1016/j.jmapro.2023.12.023>
24. K. Funaki, Y. Morisada, K. Hasegawa, T. Fukasawa, Y. Abe, H. Fujii, Weld. Int. **38**, 500–510 (2024). <https://doi.org/10.1080/09507116.2024.2335019>
25. T.J. Ma, L.F. Tang, W.Y. Li, Y. Zhang, Y. Xiao, A. Vairis, J. Manuf. Process. **34**, 442–450 (2018). <https://doi.org/10.1016/j.jmapro.2018.06.011>
26. W. Li, A. Vairis, M. Preuss, T. Ma, Int. Mater. Rev. **61**, 71–100 (2016). <https://doi.org/10.1080/09506608.2015.1109214>
27. Z. GUO, T. MA, X. YANG, J. LI, W. LI, A. VAIRIS, Chin. J. Aeronaut. **37**, 312–324 (2024). <https://doi.org/10.1016/j.cja.2023.08.018>
28. S. Rajan, P. Wanjara, J. Gholipour, A.S. Kabir, Materials **14**, 30 (2020). <https://doi.org/10.3390/ma14010030>
29. I. Bhamji, M. Preuss, P.L. Threadgill, R.J. Moat, A.C. Addison, M.J. Peel, Mater. Sci. Eng. A **528**, 680–690 (2010). <https://doi.org/10.1016/j.msea.2010.09.043>
30. R. Kuroiwa, H. Liu, Y. Aoki, S. Yoon, H. Fujii, G. Murayama, M. Yasuyama, Sci. Technol. Weld. Join. **25**, 1–9 (2020). <https://doi.org/10.1080/13621718.2019.1600771>
31. M. Orłowska, L. Olejnik, D. Campanella, G. Buffa, Ł. Morawiński, L. Fratini, M. Lewandowska, J. Manuf. Process. **56**, 540–549 (2020). <https://doi.org/10.1016/j.jmapro.2020.05.012>
32. H. Mogami, T. Matsuda, T. Sano, R. Yoshida, H. Hori, A. Hirose, Mater. Des. **139**, 457–466 (2018). <https://doi.org/10.1016/j.matdes.2017.11.043>
33. P. Geng, G. Qin, T. Li, J. Zhou, Z. Zou, F. Yang, J. Manuf. Process. **45**, 100–114 (2019). <https://doi.org/10.1016/j.jmapro.2019.06.032>
34. S. Rajan, P. Wanjara, J. Gholipour, A.S. Kabir, Materials **13**, 3664 (2020). <https://doi.org/10.3390/ma13173664>
35. P. Wanjara, B.S. Naik, Q. Yang, X. Cao, J. Gholipour, D.L. Chen, Metall. Mater. Trans. A **49**, 1641–1652 (2018). <https://doi.org/10.1007/s11661-018-4504-8>
36. P. Geng, G. Qin, H. Ma, J. Zhou, N. Ma, J. Mater. Res. Technol. **11**, 633–649 (2021). <https://doi.org/10.1016/j.jmrt.2021.01.036>
37. G. Buffa, M. Cammalleri, D. Campanella, U. La Commare, L. Fratini, Int. J. Mater. Form. **10**, 307–315 (2017). <https://doi.org/10.1007/s12289-015-1279-y>
38. I. Bhamji, R.J. Moat, M. Preuss, P.L. Threadgill, A.C. Addison, M.J. Peel, Sci. Technol. Weld. Join. **17**, 314–320 (2012). <https://doi.org/10.1179/1362171812Y.0000000010>
39. I. Bhamji, M. Preuss, R.J. Moat, P.L. Threadgill, A.C. Addison, Sci. Technol. Weld. Join. **17**, 368–374 (2012). <https://doi.org/10.1179/1362171812Y.0000000017>
40. T. Matsuda, H. Adachi, T. Sano, R. Yoshida, H. Hori, S. Ono, A. Hirose, J. Mater. Process. Technol. **269**, 45–51 (2019). <https://doi.org/10.1016/j.jmatprotec.2019.01.023>
41. F. Rotundo, A. Marconi, A. Morri, A. Ceschini, Mater. Sci. Eng. A **559**, 852–860 (2013). <https://doi.org/10.1016/j.msea.2012.09.033>
42. P. Wanjara, J. Gholipour, K. Watanabe, K. Nezaki, Y. Tian, M. Brochu, Mater. Sci. Forum. **879**, 2072–2077 (2016). <https://doi.org/10.4028/www.scientific.net/MSF.879.2072>
43. F. Ahmad Mir, N. Zaman Khan, A. Noor Siddiquee, S. Parvez, Mater. Today. Proc. **62**, 55–62 (2022). <https://doi.org/10.1016/j.matpr.2022.01.457>
44. H. Fujii, J. Light Met. Weld. **58**, 8s–13s (2020). <https://doi.org/10.11283/jlwa.58.8s>
45. A.R. McAndrew, B.C.D. Flipo, in *Proceedings of 2018 9th International Conference on Mechanical and Aerospace Engineering (ICMAE)*, Budapest, 10–13 July (IEEE, New York, 2018), pp. 126–130. <https://doi.org/10.1109/ICMAE.2018.8467692>
46. S.S.U. Islam, N.Z. Khan, A.N. Siddiquee, in *Comprehensive Materials Processing*, 2nd edn., vol.12, ed. by S. Hashmi (Elsevier, Amsterdam, 2024), pp. 41–56. <https://doi.org/10.1016/B978-0-323-96020-5.00046-7>
47. C. Leyens, M. Peters (eds.), *Titanium and Titanium Alloys: Fundamentals and Applications* (Wiley, Hoboken, 2003). <https://doi.org/10.1002/3527602119>
48. F. Scherillo, A. Astarita, L. Carrino, C. Pirozzi, U. Prisco, A. Squillace, Mater. Manuf. Process. **34**, 201–207 (2019). <https://doi.org/10.1080/10426914.2018.1532086>
49. P. Geng, G. Qin, H. Ma, J. Zhou, C. Zhang, N. Ma, J. Mater. Process. Technol. **296**, 117198 (2021). <https://doi.org/10.1016/j.jmatprotec.2021.117198>
50. Technical data sheet, Allegheny Technologies Incorporated. <https://www.atimaterials.com>
51. A.N. Siddiquee, S. Pandey, M.H. Abidi, A. Al-Ahmari, N.Z. Khan, N. Gangil, Proc. Inst. Mech. Eng. C J. Mech. Eng. Sci. **234**, 1031–1043 (2020). <https://doi.org/10.1177/0954406219888238>
52. H. Miao, T. Yamashita, S. Tsutsumi, Y. Morisada, H. Fujii, J. Adv. Join. Process. **9**, 100201 (2024). <https://doi.org/10.1016/j.jajp.2024.100201>
53. Y. Wang, S. Tsutsumi, T. Kawakubo, H. Fujii, Fatigue Fract. Eng. Mater. Struct. **45**, 2769–2783 (2022). <https://doi.org/10.1111/ffe.13772>
54. P. Sivaraj, M. Vinoth Kumar, V. Balasubramanian, in *Advances in Materials and Metallurgy: Select Proceedings of ICEMM 2018* (Springer, Singapore, 2019), pp. 467–476. [https://doi.org/10.1007/978-981-13-1780-4\\_45](https://doi.org/10.1007/978-981-13-1780-4_45)
55. A. Lis, H. Mogami, T. Matsuda, T. Sano, R. Yoshida, H. Hori, A. Hirose, J. Mater. Process. Technol. **255**, 547–558 (2018). <https://doi.org/10.1016/j.jmatprotec.2018.01.002>
56. G. Buffa, D. Campanella, A. D’Annibale, A. di Ilio, L. Fratini, Key Eng. Mater. **611–612**, 1511–1518 (2014). <https://doi.org/10.4028/www.scientific.net/KEM.611-612.1511>
57. G. Buffa, M. Cammalleri, D. Campanella, L. Fratini, Mater. Des. **82**, 238–246 (2015). <https://doi.org/10.1016/j.matdes.2015.05.070>
58. H. Hasegawa, S. Komura, A. Utsunomiya, Z. Horita, M. Furukawa, M. Nemoto, T.G. Langdon, Mater. Sci. Eng. A **265**, 188–196 (1999). [https://doi.org/10.1016/S0921-5093\(98\)01136-8](https://doi.org/10.1016/S0921-5093(98)01136-8)
59. M. Lipińska, L. Olejnik, A. Pietras, A. Rosochowski, P. Bazarnik, J. Goliński, T. Brynk, M. Lewandowska, Mater. Des. **88**, 22–31 (2015). <https://doi.org/10.1016/j.matdes.2015.08.129>
60. M.W. Mahoney, C.G. Rhodes, J.G. Flintoff, W.H. Bingel, R.A. Spurling, Metall. Mater. Trans. A **29**, 1955–1964 (1998). <https://doi.org/10.1007/s11661-998-0021-5>

61. N. Gangil, S. Maheshwari, A.N. Siddiquee, *Microstruct. Anal.* **7**, 561–577 (2018). <https://doi.org/10.1007/s13632-018-0474-x>
62. X. Zhang, W. Lui, S. Liu, Y. Yuan, Y. Deng, *Chin. J. Nonferrous Met.* **19**, 861–868 (2009). [https://caod.oriprobe.com/articles/15222321/TTP\\_curve\\_of\\_aluminum\\_alloy\\_7050.htm](https://caod.oriprobe.com/articles/15222321/TTP_curve_of_aluminum_alloy_7050.htm)
63. M. Komarasamy, K. Alagarsamy, L. Ely, R.S. Mishra, *Mater. Sci. Eng. A* **716**, 55–62 (2018). <https://doi.org/10.1016/j.msea.2018.01.026>
64. J. Yuan, S. Wang, Y. Gong, J. Chen, Effect of thermal exposure on microstructures and mechanical properties of 7050-T7451 aluminum alloy plate. Paper presented at the 11th China Association for Science and Technology (2009)
65. Y.S. Sato, H. Kokawa, M. Enomoto, S. Jogan, *Metall. Mater. Trans. A* **30**, 2429–2437 (1999). <https://doi.org/10.1007/s11661-999-0251-1>
66. X. Lu, J. Du, Q. Deng, J. Zhuang, *J. Mater. Res. Technol.* **3**, 107–113 (2014). <https://doi.org/10.1016/j.jmrt.2014.03.003>
67. X. Yang, Y. Xue, S. Wang, J. Ge, Y. Chen, Z. Zhang, J. Tang, J. Xiao, *Coatings* **12**, 1496 (2022). <https://doi.org/10.3390/coatings12101496>
68. X.L. An, B. Zhang, C.L. Chu, L. Zhou, P.K. Chu, *Mater. Sci. Eng. A* **744**, 255–266 (2019). <https://doi.org/10.1016/j.msea.2018.12.019>
69. X. Yang, T. Meng, Y. Su, X. He, Z. Guo, D. Wu, T. Ma, W. Li, *J. Mater. Res. Technol.* **29**, 4636–4649 (2024). <https://doi.org/10.1016/j.jmrt.2024.02.154>
70. Y.K. Balasubramanian Gayathri, R.L. Kumar, V.V. Ramalingam, G.S. Priyadarshini, K.S. Kumar, T.R. Prabhu, *J. Bio Tribocorros.* **8**, 98 (2022). <https://doi.org/10.1007/s40735-022-00700-1>
71. M.K. Subramanian, D. Veeman, S.S. Nallathambhi, S. Thanigainathan, *Int. J. Press. Vessels Pip.* **200**, 104787 (2022). <https://doi.org/10.1016/j.ijpvp.2022.104787>
72. R. Gaddam, B. Sefer, R. Pederson, M.-L. Antti, *IOP Conf. Ser. Mater. Sci. Eng.* **48**, 012002 (2013). <https://doi.org/10.1088/1757-899X/48/1/012002>
73. R. Boyer, E.W. Collings, G. Welsch, *Materials Properties Handbook: Titanium Alloys* (ASM International, Materials Park, 1994)
74. Y. Guo, Y. Chiu, M.M. Attallah, H. Li, S. Bray, P. Bowen, *J. Mater. Eng. Perform.* **21**, 770–776 (2012). <https://doi.org/10.1007/s11665-012-0129-z>
75. X. Boyat, D. Ballat-Durand, J. Marteau, S. Bouvier, J. Favergeon, A. Orekhov, D. Schryvers, *Mater. Charact.* **158**, 109942 (2019). <https://doi.org/10.1016/j.matchar.2019.109942>
76. G.D. Wen, T.J. Ma, W.Y. Li, S.Q. Wang, H.Z. Guo, D.L. Chen, *Mater. Sci. Eng. A* **612**, 80–88 (2014). <https://doi.org/10.1016/j.msea.2014.06.010>
77. S. Rajan, P. Wanjara, J. Gholipour, A.S. Kabir, *Materials* **14**, 3136 (2021). <https://doi.org/10.3390/ma14113136>
78. A. Astarita, F. Scherillo, M. Curioni, P. Aprea, F. Impero, A. Squillace, X. Zhou, *Mater. Manuf. Process.* **31**, 2115–2122 (2016). <https://doi.org/10.1080/10426914.2016.1151048>
79. F. Wei, B. Cheng, L.T. Chew, J.J. Lee, K.H. Cheong, J. Wu, Q. Zhu, C.C. Tan, *J. Mater. Res. Technol.* **20**, 4130–4136 (2022). <https://doi.org/10.1016/j.jmrt.2022.09.006>
80. P. Geng, H. Ma, M. Wang, G. Qin, J. Zhou, C. Zhang, Y. Ma, N. Ma, H. Fujii, *Int. J. Mach. Tools Manuf.* **191**, 104062 (2023). <https://doi.org/10.1016/j.ijmachtools.2023.104062>
81. J.W. Choi, J.-M. Su, R. Hino, M. Yamamoto, Y. Aoki, H. Fujii, *J. Mater. Res. Technol.* **26**, 4483–4494 (2023). <https://doi.org/10.1016/j.jmrt.2023.08.213>
82. T. Matsuda, H. Adachi, R. Yoshida, T. Sano, H. Hori, A. Hirose, *Mater. Today Commun.* **26**, 101700 (2021). <https://doi.org/10.1016/j.mtcomm.2020.101700>
83. V. Firouzdor, S. Kou, *Metall. Mater. Trans. A* **41**, 3238–3251 (2010). <https://doi.org/10.1007/s11661-010-0366-4>
84. A. Mishra, N. Gangil, A.N. Siddiquee, Y.S. Khan, T. Bhardwaj, D.K. Singh, *Mater. Today Proc.* (2023). <https://doi.org/10.1016/j.matpr.2023.04.672>

**Publisher's Note** Springer Nature remains neutral with regard to jurisdictional claims in published maps and institutional affiliations.

Springer Nature or its licensor (e.g. a society or other partner) holds exclusive rights to this article under a publishing agreement with the author(s) or other rightsholder(s); author self-archiving of the accepted manuscript version of this article is solely governed by the terms of such publishing agreement and applicable law.